JOURNAL OF PETROLOGY | VOLUME 42 | NUMBER 6 | PAGES 1141–1170 | 2001

High-Pressure Granulites (Retrograded Eclogites) from the Hengshan Complex, North China Craton: Petrology and Tectonic Implications

GUOCHUN ZHAO[1]*, PETER A. CAWOOD[1], SIMON A. WILDE[1] AND LIANGZHAO LU[2]

[1]TECTONICS SPECIAL RESEARCH CENTRE, SCHOOL OF APPLIED GEOLOGY, CURTIN UNIVERSITY OF TECHNOLOGY, GPO BOX U1987, PERTH, W.A. 6845, AUSTRALIA

[2]DEPARTMENT OF GEOLOGY, COLLEGE OF EARTH SCIENCES, CHANGCHUN UNIVERSITY OF SCIENCE AND TECHNOLOGY, CHANGCHUN, 130026, P.R. CHINA

RECEIVED MAY 10, 2000; REVISED TYPESCRIPT ACCEPTED OCTOBER 1, 2000

Both high- and medium-pressure granulites have been found as enclaves and boudins in tonalitic–trondhjemitic–granodioritic gneisses in the Hengshan Complex. Petrological evidence from these rocks indicates four distinct metamorphic assemblages. The early prograde assemblage (M_1) is preserved only in the high-pressure granulites and represented by quartz and rutile inclusions within the cores of garnet porphyroblasts, and omphacite pseudomorphs that are indicated by clinopyroxene + sodic plagioclase symplectic intergrowths. The peak assemblage (M_2) consists of clinopyroxene + garnet + sodic plagioclase + quartz ± hornblende in the high-pressure granulites and orthopyroxene + clinopyroxene + garnet + plagioclase + quartz in the medium-pressure granulites. Peak metamorphism was followed by near-isothermal decompression (M_3), which resulted in the development of orthopyroxene + clinopyroxene + plagioclase symplectites and coronas surrounding embayed garnet grains, and decompression-cooling (M_4), represented by hornblende + plagioclase symplectites on garnet. The THERMOCALC program yielded peak (M_2) P–T conditions of 13·4–15·5 kbar and 770–840°C for the high-pressure granulites and 9–11 kbar and 820–870°C for the medium-pressure granulites, based on the core compositions of garnet, matrix pyroxene and plagioclase. The P–T conditions of pyroxene + plagioclase symplectite and corona (M_3) were estimated at ~6·5–8·0 kbar and 750–830°C, and hornblende + plagioclase symplectite (M_4) at ~4·5–6·0 kbar and 680–790°C. The P–T conditions of the early prograde assemblage (M_1) cannot be quantitatively estimated because of the absence of modal minerals. The combination of petrographic textures, mineral compositions, metamorphic reaction history, petrogenetic grids and thermobarometric data defines a near-isothermal decompressional clockwise P–T path for the Hengshan granulites, suggesting that the Hengshan Complex underwent initial crustal thickening, subsequent exhumation, and cooling and retrogression. This tectonothermal path is considered to record a major phase of collision between two continental blocks, which resulted in the final assembly of the North China Craton at ~1·8 Ga.

KEY WORDS: *continental collision; high-pressure granulite; North China Craton;* P–T *path; symplectite*

INTRODUCTION

The Hengshan Complex in conjunction with the adjoining Wutai and Fuping Complexes is considered to represent a classic Early Precambrian orogenic belt in the North China Craton (Li *et al.*, 1990; Tian, 1991; Wang *et al.*, 1996). Of particular significance is the presence of a low-grade terrane, the Wutai Complex, between two high-grade terranes—the Hengshan and Fuping Complexes (Fig. 1). Models for the evolution of

*Corresponding author. Present address: Department of Earth Sciences, University of Hong Kong, Pokfulam Road, Hong Kong. E-mail: gzhao@hkucc.hku.hk

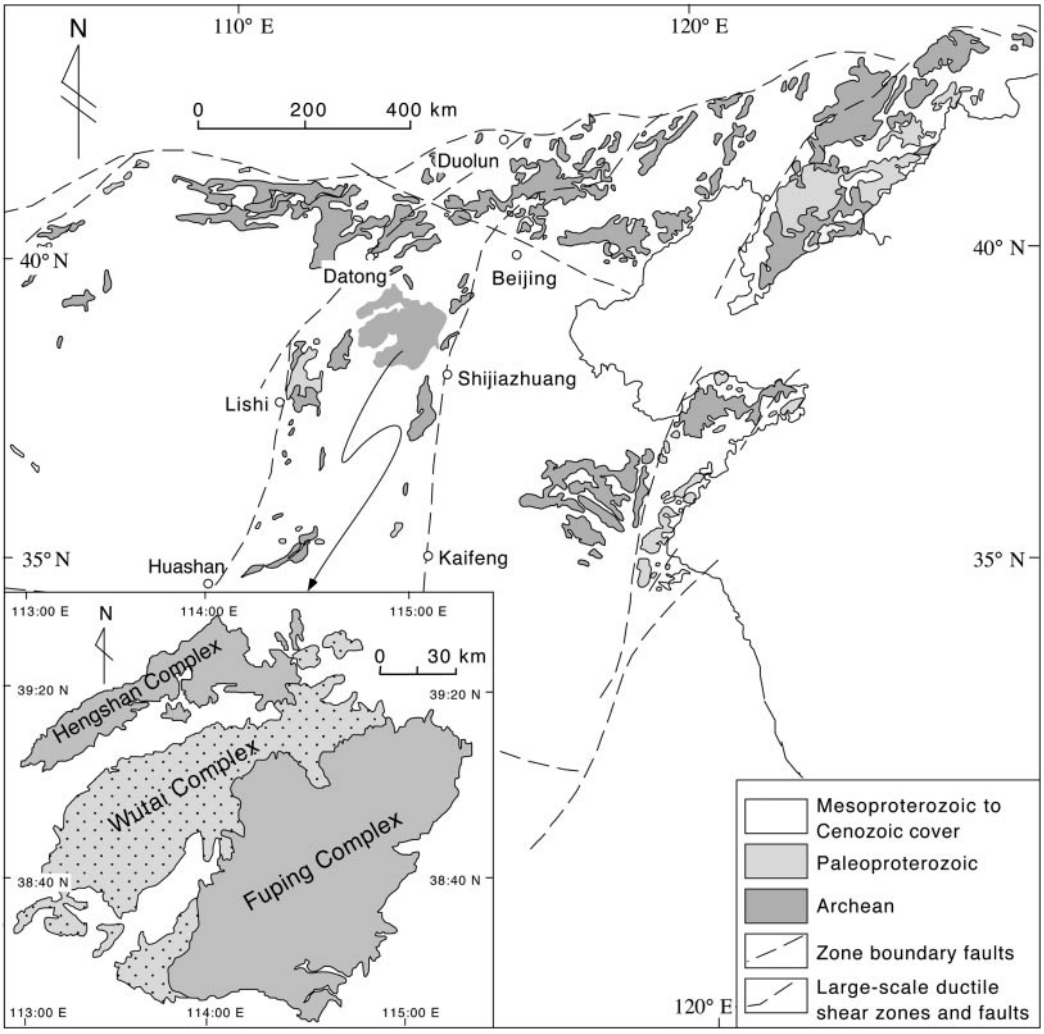

Fig. 1. Exposure of Early Precambrian rocks in the North China Craton. Inset: the spatial distribution of the Hengshan, Wutai and Fuping Complexes.

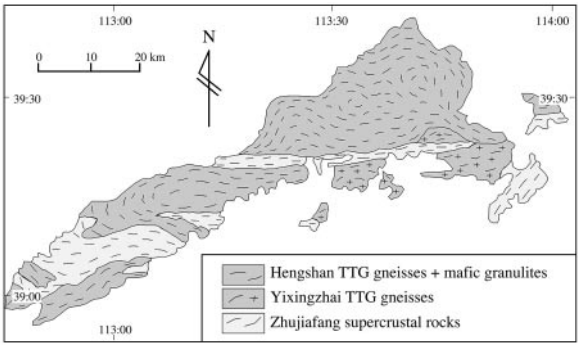

Fig. 2. Geological sketch map of the Hengshan Complexes. Line segments indicate the trends of general gneissosity.

these complexes range from those invoking an autochthonous relationship, with the Hengshan and Fuping Complexes developing on a common basement that underwent late Archaean rifting associated with formation of the Wutai sequence and closed upon itself in early Proterozoic time (Tian, 1991; Yuan & Zhang, 1993), to those proposing that the mountain belt is a late Archaean continent–arc–continent collision system in which the Fuping and Hengshan Complexes represent two exotic Archaean continental blocks and the Wutai Complex represents an intervening island arc (Li *et al.*, 1990; Bai *et al.*, 1992; Wang *et al.*, 1996). These models were based primarily on regional lithological and structural studies, combined with limited geochemical and isotopic data; few metamorphic studies have been undertaken on the major lithotectonic units within these complexes.

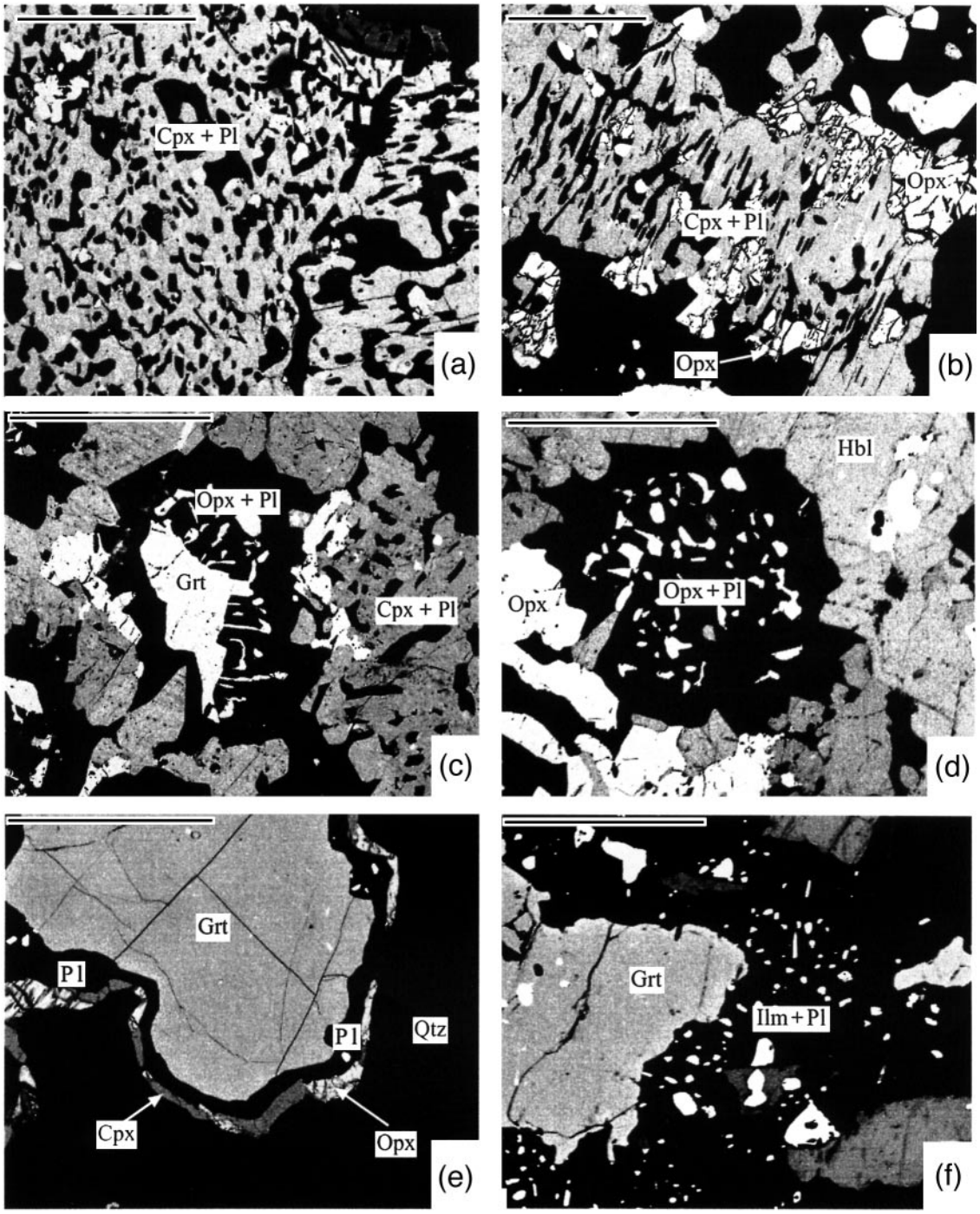

Fig. 3. Back-scattered electron images showing representative metamorphic reaction textures of the rocks studied. Scale bar represents 0·1 mm. (a) Omphacite pseudomorph indicated by sodic plagioclase + clinopyroxene symplectic intergrowths. (b) Clinopyroxene + sodic plagioclase symplectite rimmed by fine-grained orthopyroxenes. (c) Plagioclase + orthopyroxene symplectite around garnet. (d) Plagioclase + orthopyroxene symplectite existing as a pseudomorph after garnet. (e) Plagioclase + clinopyroxene + orthopyroxene corona surrounding garnet. (f) Plagioclase + ilmenite symplectite surrounding garnet. Mineral symbols are after Kretz (1983).

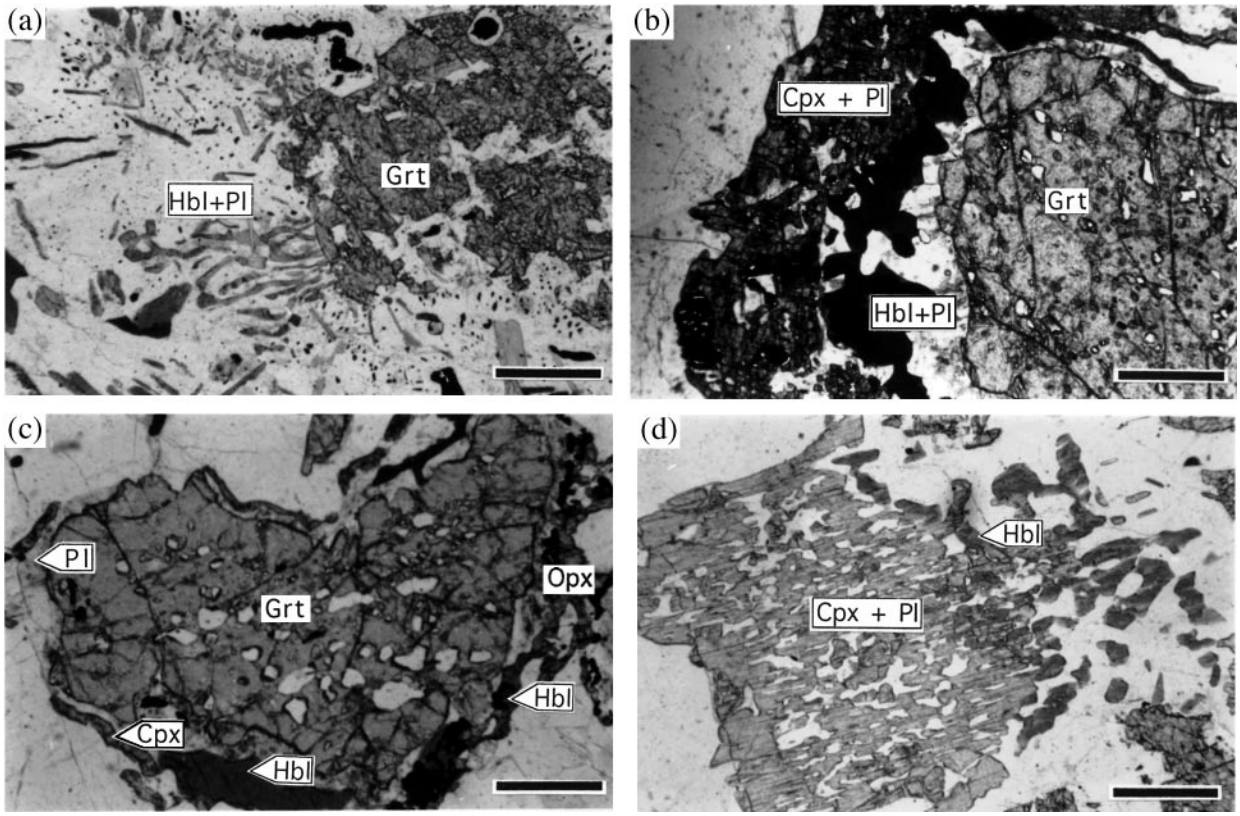

Fig. 4. Microphotographs showing representative metamorphic reaction textures of the rocks studied. Scale bar represents 0·1 mm. (a) Hornblende + plagioclase symplectite on garnet. (b) Pyroxene + plagioclase symplectic corona mantles hornblende + plagioclase symplectic corona on garnet. (c) Coronitic hornblende replacing coronitic clinopyroxene (or orthopyroxene) around garnet. (d) Matrix-type clinopyroxene and orthopyroxene replaced by hornblende rims. Mineral symbols are after Kretz (1983).

Much of the recent research in metamorphic petrology has shown that modern field- and thermodynamics-based metamorphic investigations, in combination with lithological, structural and geochronological considerations, can be directed towards understanding the tectonic setting and processes that were operative during metamorphic events (England & Thompson, 1984; Thompson & England, 1984; Sandiford & Powell, 1986; Essene, 1989; Harley, 1989; Bohlen, 1991; Brown, 1993; Vernon, 1996). Determination of *P–T* paths of metamorphism is of particular importance in this regard, because variations of pressure and temperature that characterize a metamorphic event are considered to be a function of the tectonic setting and of the heat-generating processes (England & Richardson, 1977; Oxburgh, 1989). Generally, clockwise, especially isothermal decompressional *P–T–t* paths are considered to develop in collisional environments (England & Thompson, 1984; Thompson & England, 1984; Harley, 1989; Brown, 1993), whereas anticlockwise, especially isobaric cooling *P–T–t* paths are related to the intrusion and underplating of mantle magma that can occur in continental magmatic arc regions (Wells, 1980; Bohlen, 1991), hotspots related to mantle plumes (Hill *et al.*, 1992; Zhao *et al.*, 1998, 1999*b*), or rift environments (Sandiford & Powell, 1986). Thus, investigations on the tectonothermal evolution of metamorphism can provide important constraints on the tectonic history of metamorphic complexes.

Mafic granulites and amphibolites form major lithologies within the Hengshan, Wutai and Fuping Complexes, and are particularly useful in determining metamorphic *P–T* paths because these rocks contain mineral assemblages that are well suited to estimating the pressure and temperature conditions of metamorphism and, in some cases, preserve textural evidence that can be used to infer metamorphic reaction relations and their relative timing. We have discussed the *P–T* path and tectonic implications of these rocks from the Wutai and Fuping Complexes (Zhao *et al.*, 1999*a*, 2000). This paper reports the presence of high-pressure granulites (retrograded eclogites) in the Hengshan Complex, and presents petrological and thermobarometric data

Table 1: Representative analyses of garnet

Sample:	A12	A12	B12	B12	A60	A60	A61	A61	B61	B61	A03	A03
Texture:	Type (1)											
	Core	Rim	Core	Rim	Core	Rim	Core	Rim	Core	Rim	Core	Rim
SiO_2	38·13	36·77	38·19	38·01	38·81	38·25	38·36	38·27	38·34	37·79	38·76	38·91
TiO_2	0·13	0·19	0·00	0·11	0·03	0·00	0·17	0·24	0·00	0·06	0·18	0·12
Al_2O_3	0·05	0·00	0·22	0·00	0·00	0·00	0·10	0·04	0·00	0·06	0·00	0·02
Cr_2O_3	20·80	20·60	21·24	20·93	21·24	21·27	21·06	21·23	20·52	20·54	21·25	20·98
FeO	25·08	25·07	25·03	28·77	26·55	27·89	26·64	28·05	26·68	28·04	25·94	27·20
MnO	0·75	2·64	0·55	0·69	0·52	1·30	0·48	1·51	0·67	2·54	0·74	1·09
MgO	1·91	2·31	2·09	3·41	2·43	2·73	2·65	3·11	2·32	2·11	2·76	3·04
CaO	13·14	10·40	13·97	8·74	12·03	9·59	11·74	8·73	11·67	9·50	12·04	10·60
Total	99·99	97·98	101·29	100·66	101·61	101·03	101·20	101·18	100·20	100·64	100·67	101·96
Si	3·010	2·971	2·967	2·981	3·013	2·994	2·989	2·994	3·025	2·992	3·002	3·010
Ti	0·008	0·012	0·000	0·006	0·002	0·000	0·010	0·014	0·000	0·004	0·010	0·007
Al	1·936	1·962	1·946	1·935	1·944	1·963	1·935	1·958	1·909	1·917	1·940	1·913
Cr	0·003	0·000	0·014	0·000	0·000	0·000	0·006	0·002	0·000	0·004	0·000	0·001
Fe^{3+}	0·028	0·077	0·112	0·102	0·025	0·057	0·065	0·024	0·040	0·086	0·036	0·061
Fe^{2+}	1·627	1·617	1·514	1·784	1·699	1·769	1·672	1·812	1·721	1·771	1·644	1·699
Mn	0·050	0·181	0·036	0·046	0·034	0·086	0·032	0·100	0·045	0·170	0·049	0·071
Mg	0·225	0·278	0·242	0·399	0·281	0·318	0·308	0·363	0·273	0·249	0·319	0·350
Ca	1·111	0·900	1·163	0·734	1·002	0·804	0·980	0·732	0·988	0·807	0·999	0·879
Alm	0·540	0·543	0·512	0·602	0·563	0·594	0·559	0·603	0·569	0·591	0·546	0·567
Sps	0·017	0·061	0·012	0·016	0·011	0·029	0·011	0·033	0·015	0·057	0·016	0·024
Prp	0·075	0·093	0·082	0·135	0·093	0·107	0·103	0·121	0·090	0·083	0·106	0·117
Grs	0·364	0·289	0·375	0·231	0·328	0·260	0·317	0·239	0·320	0·255	0·326	0·283
Adr	0·014	0·039	0·056	0·051	0·013	0·029	0·033	0·012	0·020	0·043	0·018	0·031

suggesting *P–T* evolution through eclogite facies into high-pressure granulite facies, and decompression through medium-pressure granulite facies and amphibolite facies. These *P–T* evolutionary processes, in combination with lithological, structural and geochronological data, place important constraints on the tectonic history of the North China Craton.

GEOLOGICAL SETTING

Regional setting and lithologies

The Hengshan–Wutai–Fuping region is located in the central part of the North China Craton, ~300 km SW of Beijing (Fig. 1). Three distinct tectonic complexes are recognized in the area: the high-grade gneiss complexes of the Hengshan in the NW and Fuping in the SE, separated by the low-grade Wutai Complex (Fig. 1). Both the Hengshan and Fuping Complexes consist of a variety of grey granitoid gneisses, amphibolites, mafic granulites and metasedimentary rocks at amphibolite- to granulite-facies metamorphic grade. The Wutai Complex is considered to be a typical granite–greenstone belt and to unconformably overlie the Fuping and Hengshan Complexes (Ma *et al.*, 1987; Tian, 1991).

The Hengshan Complex was originally considered as a series of supracrustal sequences, termed the 'Sanggan Group' or 'Hengshan Group'. The complex is composed of four lithological units (Fig. 2): the Hengshan TTG gneisses, the Hengshan mafic granulites and amphibolites, the Zhujiafang supracrustal rocks and the Yixingzhai granitoid plutons (Tian, 1991). The Hengshan TTG gneisses form >80% of the complex and underwent high-grade metamorphism and intense polyphase deformation. Petrological and geochemical data suggest that the gneisses were derived from the partial melting of mantle-derived basaltic rocks (Tian, 1986). The Zhujiafang supracrustal rocks are dominated by amphibolite, felsic gneiss,

Table 1: continued

Sample	A40	A40	B60	B60	C12	C12	A75	A75	B75	B75	A13	A13
Texture:	Type (1)				Type (2)							
	Core	Rim	Core	Rim	Core	Rim	Core	Rim	Core	Rim	Core	Rim
SiO_2	38·90	38·92	38·57	39·12	38·12	38·29	37·97	37·89	38·93	38·01	38·54	37·98
TiO_2	0·18	0·00	0·15	0·11	0·10	0·08	0·11	0·04	0·00	0·06	0·06	0·00
Al_2O_3	21·20	21·46	20·99	21·51	20·90	21·13	21·15	21·01	21·57	20·94	20·89	20·69
Cr_2O_3	0·15	0·00	0·22	0·00	0·03	0·06	0·02	0·01	0·00	0·06	0·02	0·00
FeO	27·44	26·39	27·00	27·04	26·06	27·67	26·25	28·28	25·33	28·59	26·53	29·55
MnO	0·39	1·72	0·16	1·78	0·34	0·38	1·36	1·79	0·59	1·81	0·30	0·79
MgO	2·01	3·46	2·23	3·83	2·26	3·82	3·38	3·39	4·76	3·71	3·89	3·41
CaO	11·69	9·68	12·26	8·47	12·89	9·23	10·08	7·72	9·26	6·64	10·55	7·27
Total	101·96	101·63	101·58	101·86	100·70	100·66	100·32	100·13	100·44	99·82	100·78	99·69
Si	3·020	3·014	3·002	3·021	2·983	2·993	2·978	2·995	3·020	3·000	3·000	3·018
Ti	0·011	0·000	0·009	0·006	0·006	0·005	0·006	0·002	0·000	0·004	0·004	0·000
Al	1·941	1·960	1·926	1·959	1·928	1·947	1·956	1·958	1·972	1·948	1·917	1·938
Cr	0·009	0·000	0·014	0·000	0·002	0·004	0·001	0·001	0·000	0·004	0·001	0·000
Fe^{3+}	0·000	0·013	0·038	0·000	0·101	0·054	0·078	0·045	0·000	0·079	0·075	0·028
Fe^{2+}	1·782	1·697	1·719	1·747	1·604	1·754	1·644	1·825	1·643	1·808	1·652	1·936
Mn	0·026	0·113	0·011	0·116	0·023	0·025	0·090	0·120	0·039	0·121	0·020	0·053
Mg	0·233	0·399	0·259	0·441	0·264	0·445	0·395	0·399	0·550	0·436	0·451	0·404
Ca	0·973	0·803	1·023	0·701	1·081	0·774	0·847	0·655	0·770	0·562	0·881	0·619
Alm	0·591	0·563	0·571	0·581	0·540	0·585	0·552	0·609	0·547	0·618	0·550	0·643
Sps	0·009	0·038	0·004	0·039	0·008	0·008	0·030	0·040	0·013	0·041	0·007	0·018
Prp	0·077	0·132	0·086	0·147	0·089	0·148	0·133	0·133	0·183	0·149	0·150	0·134
Grs	0·323	0·264	0·333	0·233	0·347	0·249	0·272	0·211	0·256	0·179	0·281	0·201
Adr	0·000	0·007	0·019	0·000	0·051	0·027	0·039	0·023	0·000	0·040	0·038	0·014

mica schist, banded iron formation (BIF) and quartzite. These rocks are considered to be the equivalents of the Wutai greenstone in the Hengshan area (Tian, 1991). Unlike the granulite-facies TTG gneisses, the Zhujiafang supracrustal rocks only underwent lower-amphibolite-facies metamorphism. The Yixingzhai granitoid plutons are chemically similar to the Hengshan TTG gneisses, but are only metamorphosed to greenschist to lower-amphibolite facies and are less deformed, locally preserving igneous textures. The boundaries between the Zhujiafang supracrustal rocks and the Hengshan TTG gneisses and the Yixingzhai granitoid plutons are defined by ductile shear zones (Tian, 1991).

The ages of the rock units within the Hengshan Complex as well as the timing of metamorphism have until recently been poorly constrained. Tian (1992) reported an Sm–Nd whole-rock isochron age of 2818 ± 86 Ma from mafic rock enclaves (amphibolites and medium-pressure granulites) in the Hengshan TTG gneisses and a zircon U–Pb age of 2520 ± 26 Ma from the Yixingzhai grey gneisses. The Sm–Nd age was interpreted as the age of granulite-facies metamorphism and the U–Pb age as the age of amphibolite-facies metamorphism of the Hengshan Complex (Tian, 1991, 1992; Wang *et al.*, 1996). Recent U/Pb SHRIMP dating reveals two zircon age groups within the Hengshan Complex at 2520–2550 Ma and ~1800 Ma (Wilde *et al.*, 1998; A. Kröner, personal communication, 1999), similar to the ages of the Fuping Gneisses (Wilde *et al.*, 1998). In combination with field data and new U–Pb data for the Wutai complex (Wilde *et al.*, 1997), the 2520–2550 Ma ages are thought to represent protolith ages for the Hengshan Complex, which along with the Wutai and Fuping complexes, underwent a single metamorphic

Sample:	B13	B13	C75	C75	C13	C13	13310	13301	7501	7508	7510	7511	7517
Texture:	Type (2)						Type (3)						
	Core	Rim	Core	Rim	Core	Rim	Rim	Rim	Rim	Rim	Rim	Rim	Rim
SiO_2	38·22	38·34	38·15	37·93	38·27	38·02	38·29	37·81	38·24	37·95	38·46	38·37	38·15
TiO_2	0·12	0·00	0·02	0·06	0·00	0·05	0·00	0·00	0·00	0·07	0·00	0·07	0·06
Al_2O_3	20·98	20·88	20·95	20·99	20·89	21·21	21·43	20·34	20·88	21·07	21·56	20·98	21·03
Cr_2O_3	0·09	0·19	0·04	0·23	0·01	0·09	0·08	0·00	0·03	0·00	0·07	0·07	0·19
FeO	27·88	30·06	25·65	27·99	25·51	30·06	27·86	28·63	28·19	26·58	26·51	27·77	28·15
MnO	0·68	1·07	0·84	1·28	0·46	0·87	0·52	3·38	2·03	1·87	1·39	1·95	2·04
MgO	3·07	3·67	3·85	3·70	3·02	3·51	4·04	2·75	3·17	2·95	3·69	3·21	3·67
CaO	9·51	7·12	10·71	7·90	11·81	6·78	9·19	6·98	7·80	9·54	8·67	7·68	7·20
Total	100·55	101·33	100·21	100·08	99·97	100·59	101·41	99·89	100·34	100·03	100·35	100·10	100·54
Si	3·004	2·998	2·984	2·993	2·998	2·995	2·967	3·016	3·021	2·997	3·011	3·031	3·003
Ti	0·007	0·000	0·001	0·004	0·000	0·003	0·000	0·000	0·000	0·004	0·000	0·004	0·004
Al	1·944	1·925	1·932	1·953	1·929	1·970	1·958	1·913	1·945	1·961	1·990	1·954	1·951
Cr	0·006	0·012	0·002	0·014	0·001	0·006	0·005	0·000	0·002	0·000	0·004	0·004	0·012
Fe^{3+}	0·027	0·073	0·095	0·039	0·099	0·033	0·102	0·062	0·011	0·040	0·000	0·000	0·028
Fe^{2+}	1·805	1·893	1·583	1·808	1·572	1·947	1·703	1·848	1·852	1·715	1·736	1·834	1·826
Mn	0·045	0·071	0·056	0·086	0·031	0·058	0·034	0·228	0·136	0·125	0·092	0·130	0·136
Mg	0·360	0·428	0·449	0·435	0·353	0·412	0·467	0·327	0·373	0·347	0·431	0·378	0·431
Ca	0·802	0·597	0·899	0·669	0·991	0·572	0·764	0·597	0·661	0·807	0·727	0·650	0·607
Alm	0·599	0·633	0·530	0·603	0·533	0·651	0·574	0·616	0·613	0·573	0·581	0·613	0·609
Sps	0·015	0·024	0·019	0·029	0·011	0·019	0·011	0·076	0·045	0·042	0·031	0·043	0·045
Prp	0·120	0·143	0·150	0·145	0·120	0·138	0·157	0·109	0·123	0·116	0·144	0·126	0·144
Grs	0·262	0·188	0·285	0·217	0·319	0·186	0·240	0·189	0·217	0·263	0·243	0·217	0·198
Adr	0·014	0·037	0·048	0·020	0·050	0·017	0·051	0·031	0·006	0·020	0·000	0·000	0·014

event at ~1800 Ma (A. Kröner, personal communication, 1999).

High-pressure granulites

High-pressure granulites are generally considered to represent high-grade metabasites with a main (peak) mineral assemblage of clinopyroxene + plagioclase + garnet + quartz (Yardley, 1989). They are distinguished from eclogites by the presence of plagioclase and from medium-pressure granulites by the lack of orthopyroxene in the main assemblage, although orthopyroxene may occur in high-pressure granulites as symplectites or coronas formed during post-peak decompression. Both high-pressure and medium-pressure granulites have been found in the Hengshan Complex, in which they are restricted to enclaves, boudins and sheets, ranging from 0·1 to 2 m in width and from 0·1 to 50 m in length, within the heterogeneous, veined and deformed upper-amphibolite-facies TTG gneisses. In most cases, the high- and medium-pressure granulites crop out separately; however, in some places, the high-pressure and medium-pressure granulites can be observed within the same outcrop, but they are never in contact with each other. In the field, the high-pressure granulite enclaves or boudins can be distinguished from the medium-pressure granulites by their coarse-grained textures and the lack of brown orthopyroxenes, which are ubiquitous in the medium-pressure granulite boudins. Although there are sharp contacts between the mafic granulites and the TTG gneisses, no obvious intrusive relationships have been observed between them. The long axes of the granulite enclaves or boudins are always parallel to the regional strike of the foliations of TTG gneisses. They may have been derived from metamorphosed basalts or from metamorphosed basic intrusive rocks, including gabbro and

Table 1: continued

Sample:	7518	7523	7531	1218	1220	1331	6014	6101	6121	7504	7527	7528
Texture:	Type (3)			Type (4)								
	Rim	Rim	Rim	Rim	Rim	Rim	Rim	Rim	Rim	Rim	Rim	Rim
SiO_2	38·20	38·02	38·04	37·62	38·30	38·39	38·67	38·32	38·58	37·88	37·90	38·03
TiO_2	0·00	0·08	0·05	0·00	0·00	0·00	0·06	0·12	0·00	0·07	0·00	0·00
Al_2O_3	21·11	20·73	21·38	20·95	21·10	20·79	21·24	20·84	20·92	21·04	20·88	21·18
Cr_2O_3	0·20	0·05	0·00	0·00	0·03	0·07	0·03	0·01	0·12	0·09	0·08	0·01
FeO	27·08	28·13	28·81	28·16	28·50	29·47	29·17	27·52	27·44	28·88	28·63	29·44
MnO	1·68	1·83	2·09	2·95	2·57	2·98	1·58	0·79	2·35	2·44	2·34	1·89
MgO	3·49	3·66	3·79	2·82	2·03	2·41	4·09	2·15	2·25	3·12	3·42	3·69
CaO	8·86	7·73	6·04	7·65	7·47	7·49	6·87	11·97	9·77	6·88	6·92	5·97
Total	100·62	100·23	100·20	100·15	100·00	101·72	101·71	101·72	101·43	101·40	100·17	100·21
Si	2·996	3·000	3·004	2·984	3·042	3·017	3·004	2·985	3·023	2·999	3·001	3·008
Ti	0·000	0·005	0·003	0·000	0·000	0·000	0·004	0·007	0·000	0·004	0·000	0·000
Al	1·952	1·929	1·990	1·959	1·976	1·926	1·945	1·914	1·932	1·964	1·949	1·975
Cr	0·012	0·003	0·000	0·000	0·002	0·004	0·002	0·001	0·007	0·006	0·005	0·001
Fe^{3+}	0·044	0·058	0·000	0·082	0·000	0·041	0·037	0·102	0·016	0·024	0·043	0·007
Fe^{2+}	1·732	1·799	1·903	1·786	1·893	1·895	1·858	1·691	1·782	1·888	1·854	1·941
Mn	0·112	0·122	0·140	0·198	0·173	0·198	0·104	0·052	0·156	0·164	0·157	0·127
Mg	0·408	0·430	0·446	0·333	0·240	0·282	0·474	0·250	0·263	0·368	0·404	0·435
Ca	0·745	0·654	0·512	0·650	0·636	0·631	0·572	1·000	0·820	0·584	0·588	0·507
Alm	0·578	0·599	0·634	0·602	0·643	0·630	0·618	0·565	0·590	0·628	0·617	0·645
Sps	0·037	0·041	0·047	0·067	0·059	0·066	0·035	0·017	0·052	0·055	0·052	0·042
Prp	0·136	0·143	0·149	0·112	0·082	0·094	0·158	0·084	0·087	0·123	0·135	0·145
Grs	0·241	0·208	0·171	0·205	0·216	0·210	0·184	0·317	0·269	0·190	0·189	0·167
Adr	0·022	0·029	0·000	0·041	0·000	0·020	0·019	0·051	0·008	0·012	0·022	0·004

Type (1), garnets surrounded by matrix-type plagioclase or quartz in high-pressure granulites; type (2), garnets surrounded by matrix-type plagioclase or quartz in medium-pressure granulites; type (3), garnets in contact with plagioclase + orthopyroxene symplectite or plagioclase + clinopyroxene + orthopyroxene corona; type (4), garnets in contact with plagioclase + hornblende symplectite. Cations are calculated based on 12 oxygens. Adr = $Fe^{2+}/2$; Grs = (Ca – 3Adr)/(Fe^{2+}Mg + Mn + Ca); Prp = Mg/(Fe^{2+}Mg + Mn + Ca); Sps = Mn/(Fe^{2+}Mg + Mn + Ca); Alm = Fe^{2+}/(Fe^{2+}Mg + Mn + Ca). Fe^{3+} is derived from the scheme of Droop (1987). Mineral symbols are after Kretz (1983).

dolerite dykes; the latter appears to be the most likely interpretation.

Recent data reveal that the high-pressure granulites from the Hengshan Complex are situated in a NE–SW-trending high-pressure granulite zone, several kilometres in width, in the central North China Craton. The zone extends from the Hengshan area, through the Huaian and Xuanhua, into the northern Hebei Province, a distance of ~500 km. Along this zone, high-pressure granulites have been found in the Huaian (Zhai *et al.*, 1992, 1995; Guo *et al.*, 1993), Xuanhua (Wang *et al.*, 1994) and Northern Hebei (Li *et al.*, 1998) Complexes. A high-pressure granulite sample from the Huaian Complex yielded a garnet–clinopyroxene–orthopyroxene–whole-rock Sm–Nd isochron age of 1824 ± 18 Ma (Guo *et al.*, 1993); the U–Pb zircon age of the same sample is 1833 ± 24 Ga (Guo *et al.*, 1993). A high-grade pelitic gneiss sample associated with the high-pressure granulites gave the U–Pb zircon age of 1892 ± 23 Ga (Guo *et al.*, 1993). These data are considered to represent the timing of the high-pressure metamorphic event, whereas the protolithic ages of the high-pressure granulites have not been well constrained.

PETROGRAPHY

The present study focuses on the high-pressure granulites in the Hengshan Complex, with some comments on the medium-pressure granulites from the same complex. On

Table 2: Representative analyses of plagioclase

Sample:	A12	A12	B12	B12	A60	A60	A61	A61	B61	B61	A03	A03
Texture:	Type (1)											
	Core	Rim	Core	Rim	Core	Rim	Core	Rim	Core	Rim	Core	Rim
SiO_2	64·48	57·93	64·65	61·22	65·37	60·04	66·18	63·57	65·59	61·37	66·60	57·00
TiO_2	0·11	0·00	0·00	0·09	0·03	0·07	0·00	0·00	0·00	0·14	0·02	0·00
Al_2O_3	21·73	25·54	21·67	24·29	22·64	25·18	21·15	22·62	21·03	23·98	21·05	27·20
Cr_2O_3	0·00	0·02	0·10	0·06	0·00	0·02	0·00	0·00	0·05	0·00	0·00	0·00
FeO	0·14	0·31	0·13	0·18	0·21	0·63	0·17	0·01	0·27	0·23	0·18	0·32
MnO	0·00	0·11	0·05	0·00	0·15	0·00	0·04	0·00	0·00	0·05	0·08	0·05
MgO	0·00	0·00	0·06	0·00	0·00	0·09	0·07	0·12	0·03	0·15	0·00	0·06
CaO	3·24	7·94	3·24	5·96	3·86	6·94	2·38	4·28	2·40	5·78	3·05	9·42
Na_2O	9·01	6·74	9·15	7·70	8·82	7·21	9·49	8·83	9·44	8·14	9·60	6·00
K_2O	0·27	0·41	0·02	0·42	0·61	0·33	0·69	0·35	0·63	0·51	0·04	0·23
Total	98·98	99·00	99·07	99·92	101·69	100·51	100·17	99·78	99·44	100·35	100·62	100·28
Si	2·864	2·621	2·867	2·722	2·838	2·665	2·905	2·814	2·901	2·723	2·906	2·552
Ti	0·004	0·000	0·000	0·003	0·001	0·002	0·000	0·000	0·000	0·005	0·001	0·000
Al	1·138	1·362	1·133	1·273	1·159	1·318	1·094	1·181	1·096	1·254	1·083	1·436
Cr	0·000	0·001	0·004	0·002	0·000	0·001	0·000	0·000	0·002	0·000	0·000	0·000
Fe	0·005	0·011	0·004	0·006	0·007	0·021	0·006	0·000	0·009	0·008	0·006	0·011
Mn	0·000	0·004	0·002	0·000	0·006	0·000	0·001	0·000	0·000	0·002	0·003	0·002
Mg	0·000	0·000	0·004	0·000	0·000	0·006	0·005	0·008	0·002	0·010	0·000	0·004
Ca	0·154	0·385	0·154	0·284	0·180	0·330	0·112	0·203	0·114	0·275	0·143	0·452
Na	0·776	0·591	0·787	0·664	0·743	0·621	0·808	0·758	0·809	0·700	0·812	0·521
K	0·015	0·024	0·001	0·024	0·034	0·019	0·039	0·020	0·036	0·029	0·002	0·013
An	0·16	0·39	0·16	0·29	0·19	0·34	0·12	0·21	0·12	0·27	0·15	0·46

the basis of microstructures and reaction relations between mineral phases, four mineral assemblages are recognized from the high- and medium-pressure granulites: prograde assemblage (M_1), peak assemblage (M_2), pyroxene + plagioclase symplectite or corona (M_3) and hornblende + plagioclase symplectite (M_4).

Prograde assemblage (M_1)

Like most other granulite-facies terranes around the world, much of the chemical and textural information concerning the early prograde metamorphic history in the mafic granulites from the Hengshan Complex has been lost during the subsequent annealing at the peak stage. The only preserved early prograde textures are represented by quartz and rutile inclusions within the cores of garnet porphyroblasts, and omphacite pseudomorphs that are indicated by clinopyroxene + sodic plagioclase ($An_{10–20}$) symplectic intergrowths of which the exsolution-like sodic plagioclases make up to 30–40 vol. % (Fig. 3a). Some clinopyroxene + sodic plagioclase symplectites were retrograded into fine-grained orthopyroxenes (Fig. 3b). Similar textures have also been observed in many other high-pressure granulites and retrograded eclogites, and are thought to indicate the replacement of omphacite by plagioclase and clinopyroxene formed during the transition from eclogite facies to high-pressure granulite facies (Heinrich, 1982; Rubie, 1990; Smelov & Beryozkin, 1993; Möller, 1998).

Peak assemblage (M_2)

The peak metamorphic stage (M_2) preserved in the mafic granulites is represented by the growth of relatively coarse-grained pyroxene, plagioclase, quartz and garnet in the rocks. The characteristic peak mineral assemblage is clinopyroxene + plagioclase + garnet + quartz ± hornblende for the high-pressure granulites and orthopyroxene + clinopyroxene + plagioclase + garnet + quartz ± hornblende for the medium-pressure granulites.

Table 2: continued

Sample:	A40	A40	B60	B60	C12	C12	A75	A75	B75	B75	A13	A13
Texture:	Type (1)				Type (2)							
	Core	Rim	Core	Rim	Core	Rim	Core	Rim	Core	Rim	Core	Rim
SiO_2	64·54	59·03	64·29	61·70	60·89	54·89	58·46	56·31	60·01	55·53	58·62	55·24
TiO_2	0·00	0·07	0·00	0·05	0·02	0·00	0·16	0·00	0·00	0·00	0·19	0·11
Al_2O_3	22·27	25·16	22·15	23·94	24·77	28·24	26·17	27·87	25·33	27·88	23·66	27·73
Cr_2O_3	0·00	0·07	0·02	0·13	0·07	0·17	0·21	0·07	0·11	0·00	0·03	0·11
FeO	0·07	1·00	0·10	0·41	0·60	0·21	0·00	0·14	0·00	0·39	0·81	0·28
MnO	0·05	0·01	0·03	0·06	0·00	0·00	0·00	0·05	0·03	0·00	0·00	0·07
MgO	0·24	0·29	0·15	0·08	0·11	0·00	0·04	0·00	0·00	0·17	0·07	0·00
CaO	3·38	7·04	3·67	6·13	6·52	10·71	8·29	10·35	7·17	10·99	6·54	10·41
Na_2O	9·11	7·10	9·21	7·66	7·58	5·09	6·55	5·17	7·01	4·91	6·41	4·99
K_2O	0·41	0·34	0·52	0·41	0·48	0·33	0·38	0·23	0·30	0·21	0·53	0·25
Total	100·07	100·11	100·14	100·57	101·04	99·64	100·26	100·19	99·96	100·08	96·86	99·19
Si	2·842	2·639	2·836	2·729	2·689	2·484	2·609	2·525	2·672	2·500	2·695	2·506
Ti	0·000	0·002	0·000	0·002	0·001	0·000	0·005	0·000	0·000	0·000	0·007	0·004
Al	1·156	1·326	1·152	1·248	1·289	1·507	1·377	1·473	1·330	1·480	1·283	1·483
Cr	0·000	0·002	0·001	0·005	0·002	0·006	0·007	0·002	0·004	0·000	0·001	0·004
Fe	0·002	0·034	0·003	0·014	0·020	0·007	0·000	0·005	0·000	0·013	0·028	0·009
Mn	0·002	0·000	0·001	0·002	0·000	0·000	0·000	0·002	0·001	0·000	0·000	0·003
Mg	0·016	0·019	0·010	0·005	0·007	0·000	0·003	0·000	0·000	0·011	0·005	0·000
Ca	0·159	0·337	0·173	0·291	0·308	0·519	0·396	0·497	0·342	0·530	0·322	0·506
Na	0·778	0·615	0·788	0·657	0·649	0·447	0·567	0·449	0·605	0·429	0·572	0·439
K	0·023	0·019	0·029	0·023	0·027	0·019	0·022	0·013	0·017	0·012	0·031	0·014
An	0·17	0·35	0·17	0·30	0·31	0·53	0·40	0·52	0·35	0·55	0·35	0·53

Ilmenite, apatite, rutile and magnetite are common accessory minerals in both high- and medium-pressure granulites. The minerals locally display granoblastic polygonal texture. Garnet occurs mainly as inclusion-free porphyroblasts, 1–10 mm in diameter, but is locally poikiloblastic, containing oriented inclusion tracks of rutile and elongated quartz which defines an early foliation (S_1). The preferred orientation of the prismatic minerals (orthopyroxene, clinopyroxene and amphibole) in the matrix resulted from the development of the regional gneissosity (S_2).

Pyroxene + plagioclase ± magnetite ± ilmenite symplectite and corona (M_3)

Pyroxene + plagioclase ± magnetite ± ilmenite symplectites and symplectic coronas are widespread in both the high- and medium-pressure granulites of the Hengshan Complex. They represent the M_3 metamorphic stage following peak metamorphism (M_2). The symplectic texture consists of intergrowths of fine-grained, worm-like orthopyroxene + plagioclase ± magnetite or plagioclase ± ilmenite around embayed garnet grains (Fig. 3c). Locally, the orthopyroxene + plagioclase ± magnetite symplectites completely resorb garnet grains and exist as pseudomorphs after garnets (Fig. 3d). The corona textures consist of very elongate plagioclase, clinopyroxene and/or orthopyroxnene, separating garnet and quartz, where plagioclase is always present adjacent to garnet, and the clinopyroxene and/or orthopyroxene mantles quartz (Fig. 3e). In some places, garnet is only surrounded by plagioclase + ilmenite symplectites, without symplectic orthopyroxene (Fig. 3f). These symplectic or coronitic textures have been observed in many other granulite-facies terranes and are considered to indicate a

Sample:	B13	B13	C75	C75	C13	C13	13310	13101	7501	7508	7510	7511	7517
Texture:	Type (2)						Type (3)						
	Core	Rim	Core	Rim	Core	Rim							
SiO_2	58·15	55·12	59·48	55·00	58·81	56·18	56·07	56·18	47·41	48·37	47·16	48·64	48·25
TiO_2	0·00	0·00	0·09	0·00	0·02	0·00	0·00	0·00	0·00	0·00	0·00	0·00	0·00
Al_2O_3	25·66	27·22	25·05	27·01	25·00	27·97	26·82	27·97	33·37	32·87	33·50	32·38	33·01
Cr_2O_3	0·05	0·01	0·04	0·05	0·07	0·13	0·08	0·13	0·13	0·00	0·07	0·01	0·00
FeO	0·57	0·54	0·03	1·56	0·70	0·30	0·46	0·30	0·26	0·54	0·12	0·34	0·43
MnO	0·00	0·00	0·00	0·00	0·00	0·00	0·00	0·00	0·00	0·14	0·00	0·23	0·11
MgO	0·15	0·19	0·05	0·59	0·00	0·00	0·00	0·00	0·00	0·06	0·00	0·00	0·11
CaO	7·57	9·96	7·10	10·17	7·71	10·32	9·58	10·32	17·36	16·33	17·28	16·16	16·49
Na_2O	6·39	5·36	7·53	5·43	6·96	5·61	5·35	5·61	1·63	1·97	1·93	2·46	1·85
K_2O	0·27	0·24	0·49	0·29	0·51	0·23	0·26	0·23	0·08	0·09	0·03	0·04	0·02
Total	98·81	98·64	99·86	100·10	99·78	100·74	98·62	100·74	100·24	100·37	100·09	100·26	100·27
Si	2·627	2·515	2·662	2·489	2·642	2·511	2·552	2·511	2·173	2·209	2·166	2·225	2·205
Ti	0·000	0·000	0·003	0·000	0·001	0·000	0·000	0·000	0·000	0·000	0·000	0·000	0·000
Al	1·367	1·464	1·322	1·441	1·324	1·474	1·439	1·474	1·804	1·770	1·814	1·746	1·778
Cr	0·002	0·000	0·001	0·002	0·002	0·005	0·003	0·005	0·005	0·000	0·003	0·000	0·000
Fe	0·019	0·019	0·001	0·053	0·024	0·010	0·016	0·010	0·009	0·019	0·004	0·012	0·015
Mn	0·000	0·000	0·000	0·000	0·000	0·000	0·000	0·000	0·000	0·005	0·000	0·009	0·004
Mg	0·010	0·013	0·003	0·040	0·000	0·000	0·000	0·000	0·000	0·004	0·000	0·000	0·007
Ca	0·366	0·487	0·340	0·493	0·371	0·494	0·467	0·494	0·853	0·799	0·850	0·792	0·807
Na	0·560	0·474	0·653	0·476	0·606	0·486	0·472	0·486	0·145	0·174	0·172	0·218	0·164
K	0·016	0·014	0·028	0·017	0·029	0·013	0·015	0·013	0·005	0·005	0·002	0·002	0·001
An	0·40	0·51	0·35	0·52	0·37	0·50	0·49	0·50	0·85	0·82	0·83	0·78	0·83

decompressional process following peak granulite-facies metamorphism (e.g. Harley, 1989, 1992; Kumar & Chacko, 1991; Thost *et al.*, 1991).

Hornblende + plagioclase symplectite and corona (M_4)

In addition to pyroxene + plagioclase, hornblende + plagioclase symplectites and coronas are also present in the high- and medium-pressure granulites from the Hengshan Complex. Symplectic hornblende and plagioclase formed a worm-like intergrowth adjacent to the garnet (Fig. 4a), and coronitic hornblende and plagioclase occur as an incomplete concentric shell around garnet grains (Fig. 4b). In most cases, hornblende + plagioclase symplectites or coronas in the granulites occur around those garnet grains that lack pyroxene + plagioclase symplectites or coronas. In places, however, the two kinds of symplectic corona coexist around the same garnet grain. Recognition of this coexisting relationship in other granulites has led to the suggestion that the two kinds of symplectic corona developed at constant P and T conditions and their formation is largely dependent on grain-boundary fluid compositions around the garnet (Mengel & Rivers, 1991; Kumar & Chacko, 1994), or the mineral phases adjacent to the garnet (Thost *et al.*, 1991). In the Hengshan mafic granulites, however, in domains where the two kinds of symplectic corona are present around a single garnet grain, the hornblende + plagioclase symplectic corona is invariably located adjacent to the garnet grain and is mantled by the pyroxene + plagioclase symplectite (Fig. 4b). Locally, the symplectic orthopyroxene and/or clinopyroxene grains were replaced by symplectic hornblende (Fig. 4c). In addition, matrix-type clinopyroxene and orthopyroxene grains were also replaced by hornblende retrograde rims (Fig. 4d). These textures suggest that the hornblende + plagioclase symplectic corona formed later than the

Table 2: continued

Sample:	7518	7523	7531	1218	1220	1331	6014	6101	6121	7504	7527	7528
Texture:	Type (3)			Type (4)								
SiO_2	51·72	51·77	54·71	52·49	53·55	55·87	53·03	52·74	56·48	52·56	47·68	50·84
TiO_2	0·02	0·05	0·06	0·00	0·03	0·00	0·00	0·03	0·07	0·00	0·00	0·00
Al_2O_3	30·69	30·37	28·61	30·35	30·17	27·52	28·78	29·29	27·02	30·21	33·09	31·03
Cr_2O_3	0·02	0·13	0·00	0·00	0·06	0·00	0·09	0·06	0·11	0·01	0·00	0·10
FeO	0·40	0·36	0·14	0·41	0·33	0·21	0·44	0·27	0·53	0·26	0·26	0·64
MnO	0·01	0·00	0·15	0·00	0·06	0·00	0·00	0·05	0·00	0·11	0·05	0·00
MgO	0·04	0·16	0·10	0·00	0·13	0·02	0·12	0·00	0·00	0·00	0·07	0·00
CaO	13·52	13·26	11·25	13·01	12·56	10·10	12·02	12·68	9·96	13·20	16·53	14·20
Na_2O	3·54	3·63	4·81	4·18	4·29	5·30	3·98	4·15	5·71	3·85	2·22	3·20
K_2O	0·03	0·20	0·24	0·18	0·06	0·14	0·23	0·15	0·09	0·11	0·12	0·25
Total	99·99	99·93	100·07	100·62	101·24	99·16	98·69	99·42	99·97	100·31	100·02	100·26
Si	2·348	2·354	2·467	2·369	2·395	2·529	2·429	2·405	2·541	2·377	2·189	2·313
Ti	0·001	0·002	0·002	0·000	0·001	0·000	0·000	0·001	0·002	0·000	0·000	0·000
Al	1·643	1·628	1·521	1·615	1·591	1·469	1·554	1·575	1·433	1·611	1·791	1·664
Cr	0·001	0·005	0·000	0·000	0·002	0·000	0·003	0·002	0·004	0·000	0·000	0·004
Fe	0·014	0·012	0·005	0·014	0·011	0·007	0·015	0·009	0·018	0·009	0·009	0·022
Mn	0·000	0·000	0·006	0·000	0·002	0·000	0·000	0·002	0·000	0·004	0·002	0·000
Mg	0·003	0·011	0·007	0·000	0·009	0·001	0·008	0·000	0·000	0·000	0·005	0·000
Ca	0·658	0·646	0·544	0·629	0·602	0·490	0·590	0·620	0·480	0·640	0·813	0·692
Na	0·312	0·320	0·421	0·366	0·372	0·465	0·354	0·367	0·498	0·338	0·198	0·282
K	0·002	0·012	0·014	0·010	0·003	0·008	0·013	0·009	0·005	0·006	0·007	0·015
An	0·68	0·66	0·57	0·64	0·62	0·52	0·63	0·63	0·49	0·66	0·81	0·72

Type (1), matrix-type plagioclase in high-pressure granulites; type (2), matrix-type plagioclase in medium-pressure granulites; type (3), symplectic or coronitic plagioclase associated with symplectic or coronitic orthopyroxene and/or clinopyroxene; type (4), symplectic plagioclase associated with symplectic hornblende. Cations are calculated based on eight oxygens.

pyroxene + plagioclase symplectic corona and represents an independent metamorphic episode (M_4). The difference in *P–T* conditions obtained from the two types of symplectite and corona supports this observation.

MINERAL COMPOSITIONS

Selected minerals were analysed with a Link EDS system connected to a Jeol 6400 electron microprobe at the University of Western Australia, using Link's software for ZAF correction and data processing. Analyses were performed with a 15 kV accelerating voltage, ~5 nA beam current and counting time of 30–40 s. Natural and synthetic minerals were used as standards. A representative selection of the minerals used for *P–T* calculations is included in Tables 1–5.

Garnet

Representative garnet analyses are given in Table 1. These are: (1) core and rim compositions of non-coronitic garnet surrounded by matrix-type plagioclase and quartz in the high-pressure granulites; (2) core and rim compositions of non-coronitic garnet surrounded by matrix-type plagioclase and quartz in the medium-pressure granulites; (3) rim compositions of garnet surrounded by pyroxene + plagioclase symplectites or coronas; (4) rim compositions of garnet surrounded by hornblende + plagioclase symplectites or coronas. All garnets are dominantly almandine (50–65%), with grossular (17–37%), pyrope (7–16%), and minor spessartine (1–7%) and andradite (0–5%) components. Microprobe analyses reveal three types of variations: (1) zoning patterns within individual grains; (2) variations in the chemistry of garnet cores and rims between the high- and medium-pressure granulites; (3) systematic variations between garnet rims in contact with different symplectites or coronas.

Zoning profiles of garnets surrounded by plagioclase and/or quartz in the high- and medium-pressure granulites are shown in Fig. 5. Garnet from the high-pressure granulites is characterized by a decrease in almandine and pyrope and an increase in grossular, spessartine and

Table 3: Representative analyses of clinopyroxenes

Sample:	A12	A12	B12	B12	A60	A60	A61	A61	B61	B61	A03
Texture:	Type (1)										
	Core	Rim	Core	Rim	Core	Rim	Core	Rim	Core	Rim	Core
SiO_2	51·77	51·43	52·41	51·68	52·63	52·91	53·37	52·44	52·04	55·67	52·59
TiO_2	0·01	0·16	0·15	0·15	0·02	0·07	0·00	0·12	0·27	0·01	0·12
Al_2O_3	1·41	1·19	0·81	0·67	0·92	1·35	1·11	0·81	1·12	1·38	0·86
Cr_2O_3	0·00	0·01	0·17	0·23	0·05	0·22	0·16	0·00	0·07	0·00	0·00
FeO	13·98	13·90	13·50	11·91	12·15	12·39	11·24	11·55	12·47	18·43	12·33
MnO	0·17	0·46	0·17	0·13	0·32	0·15	0·24	0·35	0·12	0·25	0·18
MgO	11·08	10·59	11·38	11·90	11·84	11·76	12·55	11·82	11·52	14·70	11·67
CaO	21·19	21·58	21·64	21·11	22·19	22·28	22·64	22·65	22·04	7·39	22·35
Na_2O	0·38	0·00	0·04	0·11	0·03	0·07	0·40	0·25	0·28	0·00	0·06
K_2O	0·04	0·00	0·03	0·18	0·00	0·14	0·00	0·03	0·00	0·07	0·00
Total	100·03	99·32	100·30	98·07	100·15	101·34	101·71	100·02	99·93	97·90	100·16
Si	1·967	1·976	1·986	1·992	1·988	1·976	1·974	1·982	1·974	2·097	1·988
Ti	0·000	0·005	0·004	0·004	0·001	0·002	0·000	0·003	0·008	0·000	0·003
Al	0·063	0·054	0·036	0·030	0·041	0·059	0·048	0·036	0·050	0·061	0·038
Cr	0·000	0·000	0·005	0·007	0·001	0·006	0·005	0·000	0·002	0·000	0·000
Fe^{3+}	0·032	0·000	0·000	0·000	0·000	0·000	0·028	0·013	0·006	0·000	0·000
Fe^{2+}	0·412	0·447	0·428	0·384	0·384	0·387	0·320	0·352	0·390	0·581	0·390
Mn	0·005	0·015	0·005	0·004	0·010	0·005	0·008	0·011	0·004	0·008	0·006
Mg	0·627	0·606	0·643	0·683	0·666	0·655	0·692	0·666	0·651	0·825	0·657
Ca	0·863	0·889	0·879	0·872	0·898	0·892	0·897	0·917	0·896	0·298	0·905
Na	0·028	0·000	0·003	0·008	0·002	0·005	0·029	0·018	0·021	0·000	0·004
K	0·002	0·000	0·001	0·009	0·000	0·007	0·000	0·001	0·000	0·003	0·000
Sum	4·000	3·992	3·991	3·994	3·992	3·994	4·000	4·000	4·000	3·874	3·992
X_{Mg}	0·603	0·575	0·600	0·640	0·634	0·629	0·684	0·654	0·625	0·587	0·628

X_{Fe} [$=Fe/(Fe + Mg)$] from rim to core (Fig. 5a). The cores of large near-euhedral grains are compositionally homogeneous with relatively flat profiles (Fig. 5a), which we interpret as having developed during the peak metamorphism. The outermost rims, $\sim$0·5 mm wide, have extremely low grossular and high almandine contents (Fig. 5a), which reflects resetting by diffusion and/or net-transfer reactions during the post-peak decompression and cooling. Garnet from the medium-pressure granulites shows almandine and grossular variation trends similar to those of garnet in the high-pressure granulites, but its spessartine and pyrope contents are nearly uniform from rim to core (Fig. 5b).

A pronounced compositional difference is present between garnets from the high-pressure and medium-pressure granulites. The cores of garnets from the high-pressure granulites have relatively higher grossular and lower almandine and pyrope contents than those of garnets from the medium-pressure granulites (Table 1). Most cores of garnets from the high-pressure granulites have >30% grossular component, with the maximum grossular content of 37·5% in sample B12 (Table 1), whereas garnets from the medium-pressure granulites contain <28% grossular component (Table 1).

There are slight variations between garnets in contact with pyroxene + plagioclase symplectites or coronas and those in contact with hornblende + plagioclase symplectites or coronas. The rim compositions of most garnet grains in contact with pyroxene + plagioclase symplectites or coronas are higher in grossular and pyrope, and lower in almandine and spessartine than those of garnet grains in contact with hornblende + plagioclase symplectites or coronas (Table 1). These compositional variations imply that the two textural garnets are likely to have re-equilibrated under different conditions.

Table 3: continued

Sample:	A03	A40	A40	B60	B60	C12	C12	A75	A75	B75	B75
Texture:	Type (1)					Type (2)					
	Rim	Core	Rim	Core	Rim	Core	Rim	Core	Rim	Core	Rim
SiO_2	52·60	52·36	53·07	52·85	51·94	52·26	53·58	53·16	52·63	52·08	53·14
TiO_2	0·12	0·29	0·10	0·16	0·19	0·13	0·01	0·10	0·13	0·10	0·16
Al_2O_3	1·53	1·76	1·03	0·81	1·22	1·19	0·64	1·07	1·08	1·15	0·71
Cr_2O_3	0·13	0·27	0·11	0·18	0·23	0·05	0·25	0·16	0·00	0·05	0·13
FeO	12·14	12·88	11·96	11·95	11·58	13·08	11·66	10·46	11·83	12·51	11·03
MnO	0·18	0·00	0·17	0·20	0·09	0·01	0·00	0·15	0·44	0·38	0·29
MgO	11·87	11·60	11·92	11·94	12·28	11·51	12·22	12·44	12·02	11·65	12·05
CaO	21·71	21·68	22·48	22·45	21·83	21·59	22·30	22·61	21·94	21·89	22·54
Na_2O	0·47	0·25	0·05	0·18	0·25	0·21	0·37	0·00	0·18	0·26	0·00
K_2O	0·12	0·06	0·00	0·01	0·05	0·18	0·03	0·07	0·04	0·00	0·06
Total	100·87	101·15	100·89	100·73	99·66	100·21	101·06	100·22	100·29	100·07	100·11
Si	1·968	1·962	1·987	1·985	1·965	1·978	1·999	1·991	1·983	1·972	1·998
Ti	0·003	0·008	0·003	0·005	0·005	0·004	0·000	0·003	0·004	0·003	0·005
Al	0·067	0·078	0·045	0·036	0·054	0·053	0·028	0·047	0·048	0·051	0·031
Cr	0·004	0·008	0·003	0·005	0·007	0·001	0·007	0·005	0·000	0·001	0·004
Fe^{3+}	0·026	0·000	0·000	0·000	0·018	0·006	0·000	0·000	0·000	0·017	0·000
Fe^{2+}	0·354	0·404	0·374	0·375	0·349	0·408	0·364	0·328	0·373	0·379	0·347
Mn	0·006	0·000	0·005	0·006	0·003	0·000	0·000	0·005	0·014	0·012	0·009
Mg	0·662	0·648	0·665	0·668	0·693	0·649	0·679	0·694	0·675	0·657	0·675
Ca	0·870	0·870	0·902	0·903	0·885	0·876	0·891	0·907	0·886	0·888	0·908
Na	0·034	0·018	0·004	0·013	0·018	0·015	0·027	0·000	0·013	0·019	0·000
K	0·006	0·003	0·000	0·000	0·002	0·009	0·001	0·003	0·002	0·000	0·003
Sum	4·000	3·998	3·988	3·997	4·000	4·000	3·997	3·982	3·997	4·000	3·981
X_{Mg}	0·6516	0·616	0·64	0·6405	0·6651	0·614	0·651	0·6791	0·6441	0·6342	0·6605

Plagioclase

Table 2 lists representative analyses of: (1) matrix-type plagioclase in the high-pressure granulites; (2) matrix-type plagioclase in the medium-pressure granulites; (3) plagioclase from pyroxene + plagioclase symplectic coronas; (4) plagioclase from hornblende + plagioclase symplectic coronas. The principal compositional features of the different textural plagioclases include the following:

(1) plagioclase in the matrix of the high-pressure granulites shows a distinct compositional zoning, varying in composition from An_{12} to An_{46}, with an oligoclase core and an andesine rim (Table 2 and Fig. 6a). The higher anorthite contents in matrix-type plagioclase are always present in the rims in contact with or close to garnet grains. Matrix-type plagioclase from the medium-pressure granulites shows core-to-rim compositional variation trends similar to those of matrix-type plagioclase from the high-pressure granulites, with an andesine core and a labradorite rim (Table 2 and Fig. 6b).

(2) Symplectic plagioclases are generally more calcic than matrix-type plagioclases and are labradorite to bytownite in composition. A symplectic plagioclase grain, occurring in association with symplectic orthopyroxenes as pseudomorph after garnet, has nearly uniform compositions of $An_{82–86}$ across the whole grain (Fig. 6c). There is no pronounced compositional difference between plagioclases from pyroxene + plagioclase symplectite and those from hornblende + plagioclase symplectites (Table 2).

(3) A plagioclase corona, 0·25 mm across and located between a large garnet crystal and coronitic clinopyroxene, shows a compositional zoning from An_{33} to An_{52}, with anorthite increasing from the contact with clinopyroxene to the garnet (Fig. 6d). Some coronitic

Sample:	A13	A13	B13	B13	C75	C75	C13	C13	13310	13101	7511	7531
Texture:	Type (2)								Type (3)			
	Core	Rim	Core	Rim	Core	Rim	Core	Rim				
SiO_2	51·92	52·60	52·36	52·13	52·48	52·67	51·65	51·97	51·81	52·02	52·09	52·16
TiO_2	0·04	0·08	0·04	0·02	0·11	0·06	0·06	0·19	0·12	0·09	0·22	0·04
Al_2O_3	1·28	1·04	1·59	0·67	0·88	0·89	1·12	1·07	1·06	0·84	1·23	0·62
Cr_2O_3	0·14	0·02	0·00	0·10	0·29	0·26	0·09	0·13	0·10	0·00	0·05	0·00
FeO	14·21	14·47	13·42	13·54	11·77	11·20	15·25	13·55	13·94	14·53	12·30	12·15
MnO	0·55	0·00	0·21	0·00	0·20	0·28	0·11	0·09	0·43	0·02	0·17	0·18
MgO	10·75	10·78	11·45	11·55	11·99	11·70	10·05	10·85	11·70	10·88	11·80	11·71
CaO	21·75	22·15	21·97	22·22	22·01	22·52	21·83	21·65	21·39	21·70	22·10	22·23
Na_2O	0·24	0·31	0·15	0·23	0·21	0·56	0·22	0·31	0·24	0·00	0·17	0·01
K_2O	0·09	0·00	0·07	0·00	0·00	0·07	0·00	0·02	0·03	0·00	0·15	0·00
Total	100·97	101·45	101·26	100·46	99·94	100·21	100·38	99·83	100·82	100·08	100·28	99·10
Si	1·962	1·977	1·964	1·971	1·984	1·982	1·973	1·982	1·953	1·984	1·966	1·992
Ti	0·001	0·002	0·001	0·001	0·003	0·002	0·002	0·005	0·003	0·003	0·006	0·001
Al	0·057	0·046	0·070	0·030	0·039	0·039	0·050	0·048	0·047	0·038	0·055	0·028
Cr	0·004	0·001	0·000	0·003	0·009	0·008	0·003	0·004	0·003	0·000	0·001	0·000
Fe^{3+}	0·034	0·017	0·014	0·041	0·000	0·030	0·014	0·000	0·056	0·000	0·018	0·000
Fe^{2+}	0·416	0·438	0·407	0·387	0·372	0·322	0·473	0·432	0·383	0·463	0·370	0·388
Mn	0·018	0·000	0·007	0·000	0·006	0·009	0·004	0·003	0·014	0·001	0·005	0·006
Mg	0·606	0·604	0·640	0·651	0·676	0·656	0·572	0·617	0·657	0·618	0·664	0·667
Ca	0·881	0·892	0·883	0·900	0·892	0·908	0·893	0·885	0·864	0·888	0·894	0·910
Na	0·018	0·023	0·011	0·017	0·015	0·041	0·016	0·023	0·018	0·000	0·012	0·001
K	0·004	0·000	0·003	0·000	0·000	0·003	0·000	0·001	0·001	0·000	0·007	0·000
Sum	4·000	4·000	4·000	4·000	3·996	4·000	4·000	3·999	4·000	3·995	4·000	3·993
X_{Mg}	0·593	0·5797	0·6113	0·6272	0·645	0·6708	0·5474	0·5882	0·6317	0·5717	0·6422	0·6322

Type (1), matrix-type clinopyroxene in high-pressure granulites; type (2), matrix-type clinopyroxene in medium-pressure granulites; type (3), coronitic clinopyroxene in high- or medium-pressure granulites. Cations are calculated based on six oxygens. $X_{Mg} = Mg/(Mg + Fe^{2+})$. Fe^{3+} is calculated following the scheme of Droop (1987).

plagioclase grains have nearly uniform compositions of labradorite.

Clinopyroxene

Both matrix-type and coronitic clinopyroxenes are salite–augite, typical of mafic granulites, and contain a low jadeite component (Table 3). The matrix-type clinopyroxenes from the high- and medium-pressure granulites show irregular zoning patterns, especially with respect to Ca, Mg and Fe, and their Al contents slightly increase from rim to core, whereas Na contents are nearly uniform (Fig. 7a and b). A clinopyroxene corona of 0·2 mm width, between coronitic plagioclase and matrix-type quartz, is compositionally homogeneous with a relatively flat compositional profile; Ca, Al and X_{Fe} slightly increase towards the rim at coronitic plagioclase, and Mg remains almost constant (Fig. 7c).

Orthopyroxene

Table 4 lists representative core and rim compositions of matrix-type orthopyroxene and the compositions of symplectic and coronitic orthopyroxene. Matrix-type orthopyroxenes occur only in the medium-pressure granulites. There is no significant difference in chemical composition between the matrix-type orthopyroxene and symplectic or coronitic orthopyroxene. Matrix-type orthopyroxenes show relatively flat profiles, with nearly

Table 4: Representative analyses of orthopyroxene

Sample:	C12	C12	A75	A75	B75	B75	A13	A13	B13	B13	C75
Texture:	Type (1)										
	Core	Rim	Core	Rim	Core	Rim	Core	Rim	Core	Rim	Core
SiO_2	49·44	51·44	50·51	51·81	50·79	50·83	50·48	51·03	50·11	50·99	50·83
TiO_2	0·00	0·00	0·04	0·10	0·00	0·15	0·00	0·00	0·00	0·04	0·05
Al_2O_3	0·71	0·42	0·62	0·58	0·63	0·90	0·48	0·64	0·37	0·45	0·67
Cr_2O_3	0·00	0·04	0·07	0·00	0·16	0·00	0·10	0·00	0·00	0·07	0·03
FeO	36·60	32·02	32·37	29·95	32·17	31·85	32·99	32·36	34·94	32·68	32·11
MnO	0·25	0·39	0·75	0·70	0·85	0·80	0·13	0·32	0·29	0·31	0·73
MgO	12·08	14·87	15·05	16·28	15·32	15·08	14·56	15·03	12·93	15·11	14·96
CaO	0·65	0·64	0·71	0·55	0·56	0·62	0·52	0·67	0·56	0·58	0·45
Na_2O	0·00	0·00	0·17	0·00	0·00	0·00	0·00	0·01	0·00	0·00	0·10
K_2O	0·01	0·00	0·04	0·00	0·04	0·00	0·06	0·00	0·00	0·00	0·09
Total	99·74	99·82	100·33	99·97	100·52	100·23	99·32	100·06	99·20	100·23	100·22
Si	1·981	2·009	1·969	2·002	1·977	1·981	1·994	1·993	2·002	1·991	1·985
Ti	0·000	0·000	0·001	0·003	0·000	0·004	0·000	0·000	0·000	0·001	0·001
Al	0·034	0·019	0·028	0·026	0·029	0·041	0·022	0·029	0·017	0·021	0·031
Cr	0·000	0·001	0·002	0·000	0·005	0·000	0·003	0·000	0·000	0·002	0·001
Fe^{3+}	0·004	0·000	0·044	0·000	0·014	0·000	0·000	0·000	0·000	0·000	0·007
Fe^{2+}	1·222	1·046	1·012	0·968	1·033	1·038	1·090	1·057	1·167	1·067	1·049
Mn	0·008	0·013	0·025	0·023	0·028	0·026	0·004	0·011	0·010	0·010	0·024
Mg	0·721	0·866	0·874	0·937	0·889	0·876	0·857	0·875	0·770	0·879	0·871
Ca	0·028	0·027	0·030	0·023	0·023	0·026	0·022	0·028	0·024	0·024	0·019
Na	0·000	0·000	0·013	0·000	0·000	0·000	0·000	0·001	0·000	0·000	0·008
K	0·001	0·000	0·002	0·000	0·002	0·000	0·003	0·000	0·000	0·000	0·004
Sum	4·000	3·981	4·000	3·982	4·000	3·994	3·995	3·993	3·990	3·996	4·000
X_{Mg}	0·371	0·453	0·463	0·492	0·463	0·458	0·440	0·453	0·398	0·452	0·454

uniform compositions in most parts of the grains. However, across the outermost rims (~0·25 mm wide), X_{Fe} and Fe contents decrease whereas Mg contents slightly increase and Al contents remain constant (Fig. 7d). An orthopyroxene corona, 0·2 mm across, separating matrix-type quartz and coronitic plagioclase surrounding a large garnet, shows a compositional profile essentially similar to that of matrix-type orthopyroxene (Fig. 7e). A worm-like symplectic orthopyroxene, ~0·2 mm long, has nearly uniform X_{Fe}, Fe, Mg and Al contents (Fig. 7f).

Hornblende

Hornblende analyses were divided into three groups: (1) dark cores of matrix-type hornblendes; (2) light rims of matrix-type hornblendes; (3) symplectic hornblendes associated with symplectic plagioclases. Representative analyses are listed in Table 5. There is a marked difference in compositions between the core and rim of matrix hornblende. According to the nomenclature of Leake (1997), the core compositions of matrix hornblendes range from tschermakitic, through edenitic, to magnesio-hornblende, whereas the rim compositions range from ferro-edenitic hornblende, through ferropargasite, to magnesian hastingsite. The core of matrix-type hornblende is higher in SiO_2 and MgO but lower in Al_2O_3 than the rim (Table 5 and Fig. 8a). Variations in core-to-rim compositions could reflect partial re-equilibration of the cores during the post-peak thermal events (i.e. M_3 and/or M_4). Symplectic hornblende has compositions between the core and rim composition of the matrix-type hornblende, ranging from pargasitic hornblende, through magnesio-hornblende, to magnesio-hastingsite.

Sample:	C75	C13	C13	13310	13101	7501	7508	7510	7517	7518	7523
Texture:	Type (1)			Type (2)							
	Core	Rim	Core								
SiO_2	50·78	50·19	50·75	50·22	50·74	51·04	51·02	51·16	51·27	51·21	51·42
TiO_2	0·24	0·06	0·00	0·11	0·11	0·05	0·00	0·08	0·01	0·00	0·07
Al_2O_3	0·51	0·55	0·75	0·75	0·58	0·79	0·77	0·80	1·03	1·04	0·85
Cr_2O_3	0·05	0·04	0·00	0·03	0·16	0·15	0·23	0·00	0·04	0·00	0·01
FeO	32·11	36·01	33·58	34·01	35·03	31·89	32·11	31·62	30·59	31·26	31·49
MnO	0·78	0·27	1·27	1·23	0·19	0·63	0·55	0·66	0·90	0·89	0·56
MgO	15·04	12·86	13·90	13·62	13·68	14·88	15·16	15·23	15·61	15·32	14·83
CaO	0·61	0·72	0·77	0·56	0·68	0·63	0·59	0·52	0·51	0·56	0·60
Na_2O	0·00	0·00	0·08	0·00	0·00	0·00	0·00	0·00	0·00	0·00	0·00
K_2O	0·01	0·00	0·13	0·00	0·00	0·02	0·00	0·00	0·01	0·03	0·00
Total	100·13	100·70	101·23	100·53	101·17	100·08	100·43	100·07	99·97	100·31	99·83
Si	1·985	1·984	1·977	1·977	1·984	1·991	1·985	1·992	1·990	1·987	2·003
Ti	0·007	0·002	0·000	0·003	0·003	0·001	0·000	0·002	0·000	0·000	0·002
Al	0·024	0·026	0·034	0·035	0·027	0·036	0·035	0·037	0·047	0·048	0·039
Cr	0·002	0·001	0·000	0·001	0·005	0·005	0·007	0·000	0·001	0·000	0·000
Fe^{3+}	0·000	0·002	0·023	0·003	0·000	0·000	0·000	0·000	0·000	0·000	0·000
Fe^{2+}	1·050	1·189	1·071	1·117	1·146	1·040	1·045	1·030	0·993	1·015	1·026
Mn	0·026	0·009	0·042	0·041	0·006	0·021	0·018	0·022	0·030	0·029	0·018
Mg	0·876	0·758	0·807	0·799	0·797	0·865	0·879	0·884	0·903	0·886	0·861
Ca	0·026	0·031	0·032	0·024	0·029	0·026	0·025	0·022	0·021	0·023	0·025
Na	0·000	0·000	0·006	0·000	0·000	0·000	0·000	0·000	0·000	0·000	0·000
K	0·000	0·000	0·006	0·000	0·000	0·001	0·000	0·000	0·000	0·001	0·000
Sum	3·995	4·000	4·000	4·000	3·997	3·987	3·994	3·988	3·986	3·990	3·975
X_{Mg}	0·455	0·389	0·430	0·417	0·410	0·454	0·457	0·462	0·476	0·466	0·456

Type (1), matrix-type orthopyroxene in medium-pressure granulites; type (2), symplectic or coronitic orthopyroxene in high- or medium-pressure granulites. $X_{Mg} = Mg/(Mg + Fe^{2+})$. Cations are calculated based on six oxygens. Fe^{3+} is calculated following the scheme of Droop (1987).

Small worm-like symplectic hornblende grains are unzoned towards the grain boundaries with embayed garnet grains (Fig. 8b).

REACTION HISTORY

In the high-pressure granulites, the Ca-rich garnet and sodic plagioclase + clinopyroxene symplectites, with up to 30–40 vol. % exsolution-like sodic plagioclase (Fig. 3a), provide evidence that eclogitic assemblages developed during an early stage of metamorphism, followed by high-pressure granulite-facies metamorphism. Sodic plagioclase + clinopyroxene symplectites can be explained by a breakdown of jadeite-rich clinopyroxene (omphacite) through the following solid–solid reaction during the transition from eclogite facies to high-pressure facies (Heinrich, 1982; Rubie, 1990; Smelov & Beryozkin, 1993; Möller, 1998):

$$\text{omphacite} + \text{quartz} \rightarrow \text{sodic plagioclase} + \text{clinopyroxene}. \quad (1)$$

The phase relationships of this reaction can be chemographically interpreted in terms of Al_2O_3–(CaO + Na_2O)–(FeO + MgO)–SiO_2 space (Fig. 9a). This reaction texture has also been found in many other high-pressure granulites and retrograded eclogites (Heinrich, 1982; O'Brien, 1989; Rubie, 1990; Smelov & Beryozkin, 1993; Möller, 1998). Smelov & Beryozkin (1993) tried to quantitatively estimate the jadeite contents of the original omphacite in the Olekma retrograded eclogites by calculating the compositions and relative proportions of

Table 5: Representative analyses of hornblende

Sample:	A12	A12	B12	B12	A61	A61	B61	B61	A40	A40
Texture:	Type (1)									
	Core	Rim	Core	Rim	Core	Rim	Core	Rim	Core	Rim
SiO_2	41·97	40·40	44·45	43·24	42·50	41·04	43·71	42·52	42·22	41·41
TiO_2	1·91	1·13	1·87	1·13	1·77	1·23	1·57	1·51	1·81	1·77
Al_2O_3	11·87	13·68	8·82	14·20	11·74	12·67	9·93	12·02	12·16	13·18
Cr_2O_3	0·05	0·00	0·00	0·18	0·23	0·27	0·20	0·12	0·23	0·09
FeO	19·27	20·58	18·65	17·06	19·28	19·29	18·69	19·76	19·10	19·26
MnO	0·07	0·10	0·14	0·03	0·07	0·15	0·00	0·08	0·03	0·06
MgO	9·11	7·72	9·43	7·13	9·65	8·38	10·08	9·03	8·95	8·37
CaO	11·41	11·22	12·74	10·43	11·54	11·52	11·50	11·45	11·40	11·85
Na_2O	1·68	1·35	1·37	2·02	1·87	1·21	1·42	1·41	1·43	1·66
K_2O	1·36	1·57	1·01	2·14	1·20	1·55	1·02	1·27	1·37	1·37
Total	98·70	97·75	98·48	97·56	99·85	97·31	98·12	99·17	98·70	99·02
Si	6·271	6·109	6·589	6·499	6·263	6·217	6·512	6·299	6·292	6·186
Ti	0·215	0·129	0·208	0·128	0·196	0·140	0·176	0·168	0·203	0·199
Al^{IV}	1·729	1·891	1·411	1·501	1·737	1·783	1·488	1·701	1·708	1·814
Al^{VI}	0·362	0·548	0·13	1·015	0·303	0·48	0·256	0·398	0·428	0·507
Cr	0·006	0·000	0·000	0·021	0·027	0·032	0·024	0·014	0·027	0·011
Fe^{3+}	0·477	0·687	0·728	0·033	0·551	0·581	0·533	0·609	0·471	0·373
Fe^{2+}	1·931	1·915	1·584	2·112	1·825	1·863	1·796	1·840	1·910	2·034
Mn	0·009	0·013	0·018	0·004	0·009	0·019	0·000	0·010	0·004	0·008
Mg	2·029	1·740	2·083	1·597	2·119	1·892	2·238	1·994	1·988	1·864
Ca	1·827	1·818	2·024	1·680	1·822	1·870	1·836	1·817	1·820	1·897
Na^{M4}	0·173	0·182	−0·024	0·32	0·178	0·13	0·164	0·183	0·18	0·103
Na^{A}	0·314	0·214	0·418	0·269	0·356	0·225	0·246	0·222	0·233	0·378
K	0·260	0·303	0·191	0·411	0·226	0·300	0·194	0·240	0·261	0·261
Sum	15·601	15·549	15·360	15·588	15·612	15·532	15·464	15·495	15·525	15·634

clinopyroxene and plagioclase in a symplectic intergrowth. This approach may not be reliable because the clinopyroxene + sodic plagioclase symplectic texture does not reflect an isochemical exsolution, but involves reactions with quartz, and also, in most cases, the rims of clinopyroxene + plagioclase symplectites have reacted to orthopyroxene + plagioclase symplectites during post-peak decompression (Möller, 1998).

In the medium-pressure granulites, the actual metamorphic reactions for the formation of the peak mineral assemblage orthopyroxene + clinopyroxene + plagioclase + quartz + garnet cannot be determined because of the lack of the early prograde minerals. In a few cases, some relict hornblende inclusions have been found within garnet porphyroblasts and coarse-grained orthopyroxene and clinopyroxene grains. This suggests that the following general metamorphic reactions may have occurred during peak metamorphism:

$$\text{hornblende} + \text{plagioclase} + \text{quartz} + \text{magnetite} \rightarrow \text{clinopyroxene} + \text{garnet} + H_2O + O_2 \quad (2)$$

$$\text{hornblende} + \text{quartz} \rightarrow \text{orthopyroxene} + \text{clinopyroxene} + \text{plagioclase} + H_2O \quad (3)$$

$$\text{hornblende} + \text{quartz} \rightarrow \text{orthopyroxene} + \text{plagioclase} + H_2O. \quad (4)$$

Reaction zones between garnet and quartz, with formation of the orthopyroxene + plagioclase ± magnetite symplectites and clinopyroxene + plagioclase ± orthopyroxene coronas in both the high- and medium-pressure granulites, suggest a combination of the following reactions:

Sample:	1218	1220	1331	6014	6101	6121	7504	7527	7528
Texture:	Type (2)								
SiO_2	40·94	42·32	40·89	47·42	41·25	42·00	44·61	45·22	45·46
TiO_2	1·13	1·92	1·31	0·45	0·96	1·27	1·24	1·09	0·79
Al_2O_3	13·44	11·06	12·88	9·03	13·34	13·19	10·72	11·05	10·51
Cr_2O_3	0·00	0·03	0·02	0·15	0·20	0·16	0·11	0·00	0·19
FeO	19·19	18·52	18·76	17·21	19·70	19·08	19·25	18·20	18·70
MnO	0·00	0·09	0·20	0·09	0·22	0·05	0·15	0·25	0·13
MgO	8·29	8·98	8·34	11·71	8·35	8·69	9·98	10·17	10·41
CaO	11·23	11·29	11·24	11·40	11·61	11·73	11·66	11·64	11·86
Na_2O	1·25	1·60	1·45	0·91	1·45	1·49	1·39	1·42	1·14
K_2O	1·58	1·17	1·67	0·67	1·28	1·34	0·87	0·80	0·62
Total	97·05	96·98	96·76	99·04	98·36	99·00	99·98	99·84	99·81
Si	6·200	6·417	6·238	6·87	6·172	6·238	6·504	6·574	6·587
Ti	0·129	0·219	0·15	0·049	0·108	0·142	0·136	0·119	0·086
Al^{IV}	1·800	1·583	1·762	1·130	1·828	1·762	1·496	1·426	1·413
Al^{VI}	0·600	0·394	0·554	0·412	0·525	0·548	0·347	0·468	0·382
Cr	0·000	0·004	0·002	0·017	0·024	0·019	0·013	0·000	0·022
Fe^{3+}	0·567	0·371	0·431	0·476	0·653	0·477	0·606	0·477	0·677
Fe^{2+}	1·864	1·977	1·963	1·609	1·812	1·893	1·741	1·736	1·589
Mn	0·000	0·012	0·026	0·011	0·028	0·006	0·019	0·031	0·016
Mg	1·871	2·029	1·896	2·528	1·862	1·924	2·169	2·203	2·248
Ca	1·822	1·834	1·837	1·770	1·861	1·867	1·822	1·813	1·841
Na^{M4}	0·178	0·166	0·163	0·23	0·139	0·133	0·178	0·187	0·159
Na^{A}	0·189	0·304	0·266	0·026	0·282	0·296	0·215	0·213	0·161
K	0·306	0·227	0·325	0·124	0·245	0·254	0·162	0·149	0·115
Sum	15·525	15·537	15·614	15·253	15·538	15·559	15·407	15·396	15·297

Type (1), matrix-type hornblende in high-pressure granulites; type (2), symplectic hornblende in high- or medium-pressure granulites. Cations are calculated based on 23 oxygens. F and Cl contents in hornblende are below detection limit. Fe^{3+} is calculated following the scheme of Droop (1987).

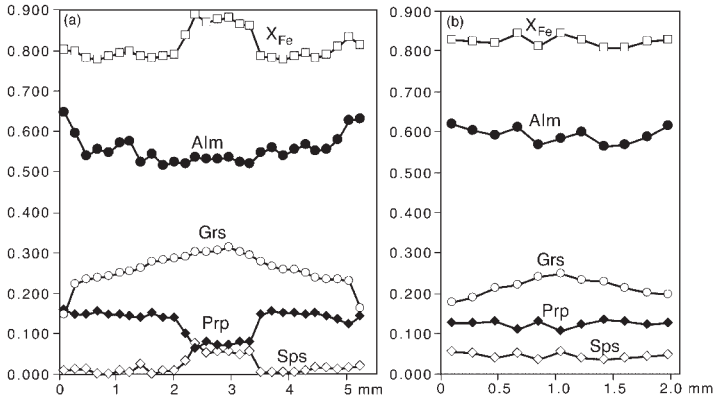

Fig. 5. Representative compositional zoning profiles of garnet. (a) Rim to rim in high-pressure granulites (next to clinopyroxene + orthopyroxene + plagioclase corona at both rims). (b) Rim to rim in medium-pressure granulites (next to plagioclase + quartz at both rims).

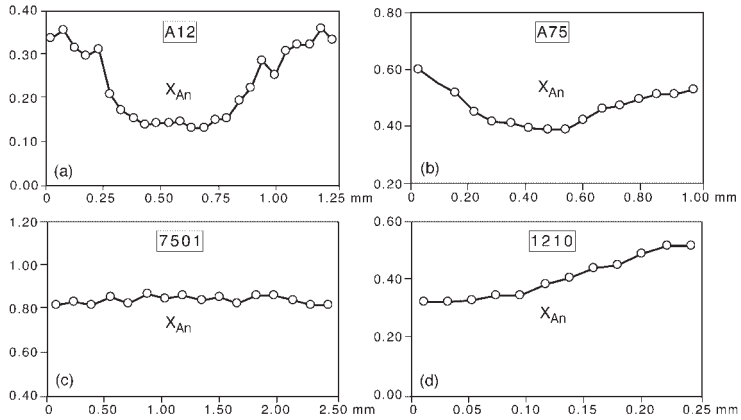

Fig. 6. Representative compositional zoning profiles of plagioclase. (a) A matrix-type plagioclase grain between clinopyroxene grains in high-pressure granulite sample A12. (b) A matrix-type plagioclase grain between quartz (right) and clinopyroxene (left). (c) A symplectic plagioclase grain associated with orthopyroxene as a pseudomorph after garnet porphyroblasts. (d) A coronitic plagioclase grain between garnet (right) and clinopyroxene (left).

garnet + quartz → orthopyroxene + plagioclase (5)

garnet + quartz ± O_2 → orthopyroxene + plagioclase ± magnetite (6)

garnet + clinopyroxene + quartz ± O_2 → orthopyroxene + plagioclase ± magnetite (7)

garnet + quartz → clinopyroxene + plagioclase. (8)

Reactions (5), (6) and (7) can also be shown chemographically in Al_2O_3–(CaO + Na_2O)–(FeO + MgO)–SiO_2 projection system (Fig. 9b). These reactions are strongly pressure dependent and proceed to the right with decompression. Reactions (5) and (8) have been calibrated as classic barometers (Newton & Perkins, 1982; Perkins & Chipera, 1985; Moecher *et al.*, 1988; Essene, 1989).

Plagioclase + ilmenite symplectites surrounding embayed garnet grains suggest the following reaction:

garnet + rutile → ilmenite + plagioclase + quartz. (9)

The chemographic phase relations of this reaction can be explained in terms of the SiO_2–CaO–FeO–TiO_2 tetrahedron projection system (Fig. 9c). This pressure-sensitive reaction has also been calibrated as a barometer (Bohlen & Liotta, 1986) and proceeds to the right on decompression.

Hornblende + plagioclase ± magnetite symplectites or coronas, although volumetrically subordinate to the orthopyroxene + plagioclase ± magnetite symplectites or coronas, are nevertheless widespread in both the high- and medium-pressure granulites of the Hengshan Complex. Their formation has been related to the following two reactions by Harley (1989) and Mengel & Rivers (1991):

garnet + clinopyroxene + quartz + H_2O ± O_2 → plagioclase + hornblende ± magnetite (10)

$garnet_1$ + $plagioclase_1$ + quartz + H_2O → $garnet_2$ + $plagioclase_2$ + hornblende. (11)

The phase relations of reaction (10) are shown in Fig. 9d. Both reactions (10) and (11) require the presence of some water, suggesting that their occurrence depends on fluid compositions as well as *P–T* conditions.

All of the observed reactions are typical of decompression and retrogression, suggesting a clockwise *P–T* history, progressing through eclogite facies, decompressing and cooling through high- and medium-granulite facies, to amphibolite facies.

P–T EVOLUTION CONSTRAINED BY PETROGENETIC GRIDS

The petrogenetic (or *P–T*) grids of metamafic rocks have been investigated using essentially two different approaches. Some workers calculate stable N_2O–CaO–FeO–MgO–Al_2O_3–SiO_2–H_2O (NCFMASH) system reactions using experimentally based, internally consistent thermodynamic datasets for the mineral end-members, combined with estimated solution models (e.g. Hansen, 1981; Holland & Powell, 1998), whereas others establish reaction grids based on repeated occurrences of natural mineral assemblage sequences, combined with Schreinemakers' rules (e.g. Mueller & Saxena, 1977). In this study, the *P–T* grid of Holland & Powell (1998) is used because it was constructed based on the updated thermodynamic data and solution models, and it agrees well with the sequence of mineral reactions deduced for

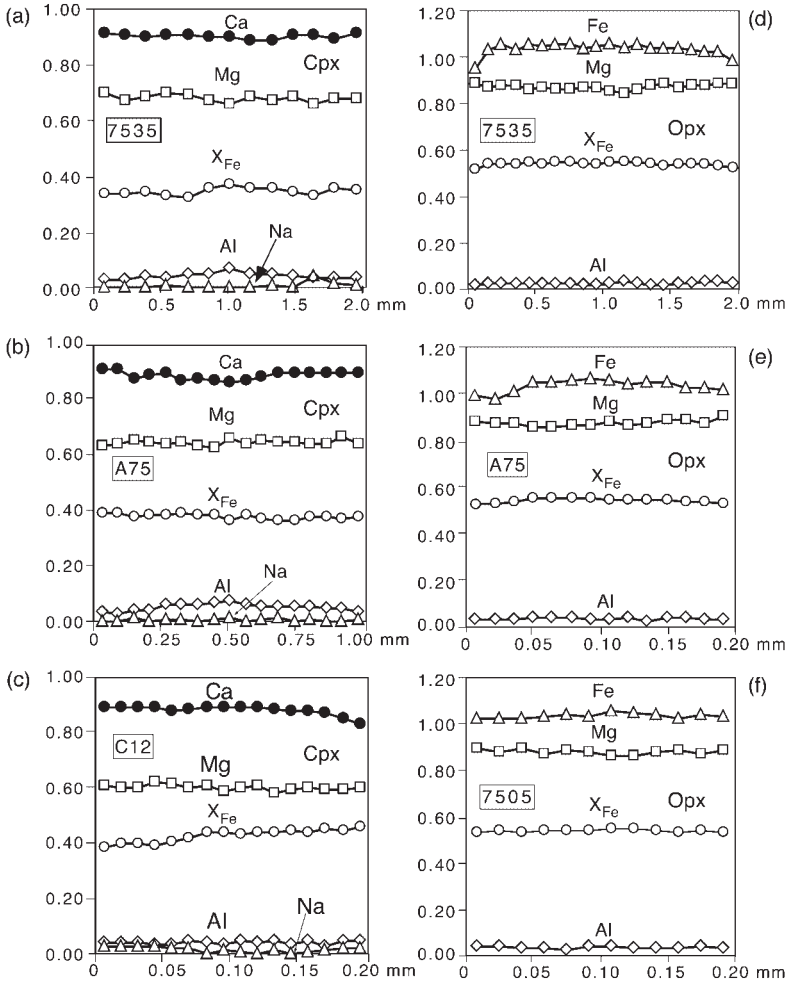

Fig. 7. Representative compositional zoning profiles of pyroxenes. (a) A matrix-type clinopyroxene grain between plagioclase (right) and quartz (left) in high-pressure granulites. (b) A matrix-type clinopyroxene grain between quartz (right) and orthopyroxene (left) in medium-pressure granulites. (c) A coronitic clinopyroxene grain between coronitic plagioclase (right) and matrix-type quartz (left). (d) A matrix-type orthopyroxene grain between plagioclase (right) and clinopyroxene (left) in medium-pressure granulites. (e) A coronitic orthopyroxene grain between coronitic plagioclase (right) and matrix-type quartz (left). (f) A symplectic orthopyroxene grain associated with orthopyroxene as a pseudomorph after garnet porphyroblasts.

the high- and medium-pressure mafic granulites in the Hengshan Complex.

Figure 10 is a *P–T* pseudosection of the NCFMAS grid of Holland & Powell (1998), but extension for low-temperature domains has been made to take into account the hornblende + plagioclase symplectite assemblage (M_4) observed in the mafic granulites of the Hengshan Complex. This NCFMAS (+ quartz) grid was built up for a silica-saturated aluminous basalt bulk composition (in wt %, SiO_2, 54·5; Al_2O_3, 19·2; CaO, 8·4; MgO, 6·0; FeO, 8·2; Na_2O, 3·7) with <0·5% normative quartz. Compared with the chemical compositions of the mafic granulites from the Hengshan Complex, this model NCFMAS composition is higher in SiO_2, Al_2O_3 and Na_2O. Despite these compositional variations, the calculated *P–T* pseudosection of the NCFMAS grid shows a sequence of mineral assemblages similar to those observed in the Hengshan high- and medium-pressure granulites, except for the presence of kyanite, which is not present in the Hengshan mafic granulites, probably because of their lower Al_2O_3 contents than the model NCFMAS composition. For example, the fields garnet + omphacite + kyanite, garnet + clinopyroxene + plagioclase, garnet + clinopyroxene + orthopyroxene + plagioclase and clinopyroxene + orthopyroxene + plagioclase in the pseudosection, each of which is with quartz in excess, can be used to show the prograde assemblage (M_1), the peak assemblages (M_2) in the

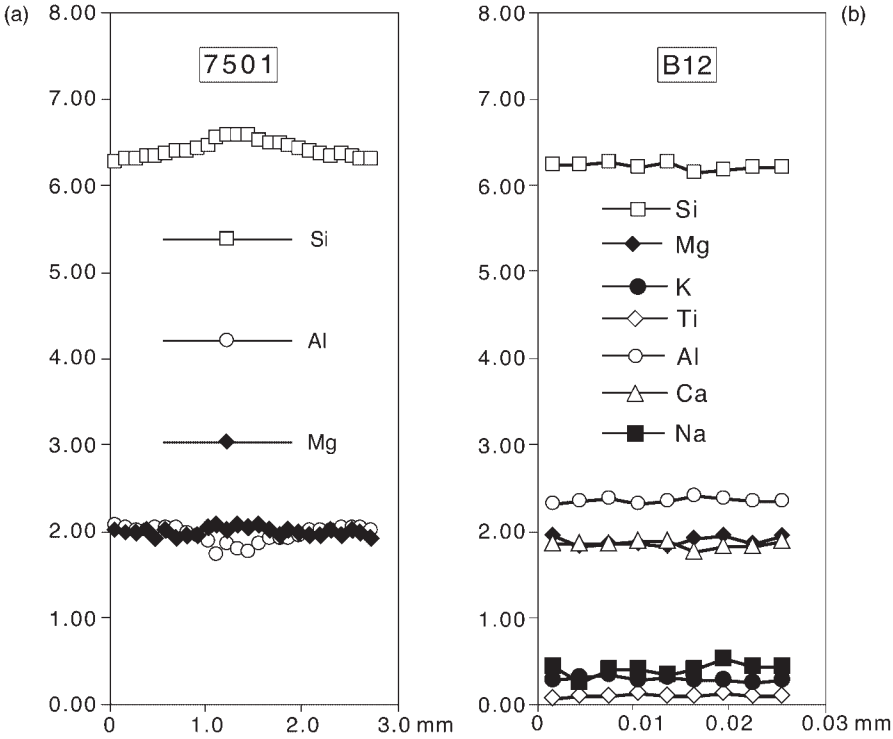

Fig. 8. Representative compositional zoning profiles of hornblende. (a) A matrix-type hornblende grain between plagioclase (right) and clinopyroxene (left) in high-pressure granulites. (b) A symplectic hornblende grain between plagioclase (right) and quartz (left) in medium-pressure granulites.

high-pressure granulites, the peak assemblages (M_2) in the medium-pressure granulites, and the orthopyroxene + plagioclase + clinopyroxene corona and symplectite assemblage (M_3) in the Hengshan mafic granulites, respectively (Fig. 10). As seen in Fig. 10, at the temperature range between 700 and 850°C, the equilibrium pressure conditions of the field garnet + omphacite (+ kyanite) are certainly higher than those of both high-pressure granulite field clinopyroxene + garnet + sodic plagioclase and medium-pressure granulite field orthopyroxene + clinopyroxene + garnet + plagioclase, and thus, the transition from the early prograde assemblage (M_1) to the peak assemblage (M_2) represents a decompressional process. Similarly, the transition from the peak assemblage (M_2) to the orthopyroxene + clinopyroxene + plagioclase corona and symplectite assemblage (M_3) also mainly reflects a decompressional process (Fig. 10).

Figure 10 also shows the 'hornblende-out' (often corresponds to 'orthopyroxene-in') curve. The location of this curve was not well constrained by experimental data, but was generalized by Baker (1990) mainly on the basis of petrographic observation, geothermometry and geobarometry. The field showing the hornblende + plagioclase symplectite assemblage should be present on the left side of this curve, assuming that the location of the curve is correct, and therefore, the transition from M_3 to M_4 should be characterized by cooling, accompanied simultaneously with decompression. Taken together, a clockwise *P–T* path has been qualitatively inferred according to the sequence of different mineral assemblages in the Hengshan high- and medium-pressure granulites. The quantitative *P–T* trajectory cannot be defined from this *P–T* pseudosection because of the lack of sufficient reactions and the difference between the model and actual chemical compositions.

QUANTITATIVE *P–T* ESTIMATES

Quantitative estimates of the early prograde metamorphic assemblage (M_1) cannot be made because of the absence of modal minerals for this assemblage. The peak assemblage (M_2), pyroxene + plagioclase corona and symplectite (M_3) and hornblende + plagioclase symplectite (M_4) have potential for quantitative *P–T* evaluation because of the possibility of equilibrium between core compositions of the peak minerals and local equilibrium between the re-equilibrated garnet rim and the newly formed symplectic or coronitic clinopyroxene, orthopyroxene, plagioclase and hornblende. The *P–T* estimates based on these mineral compositions should define a *P–T* path consistent with the above qualitative

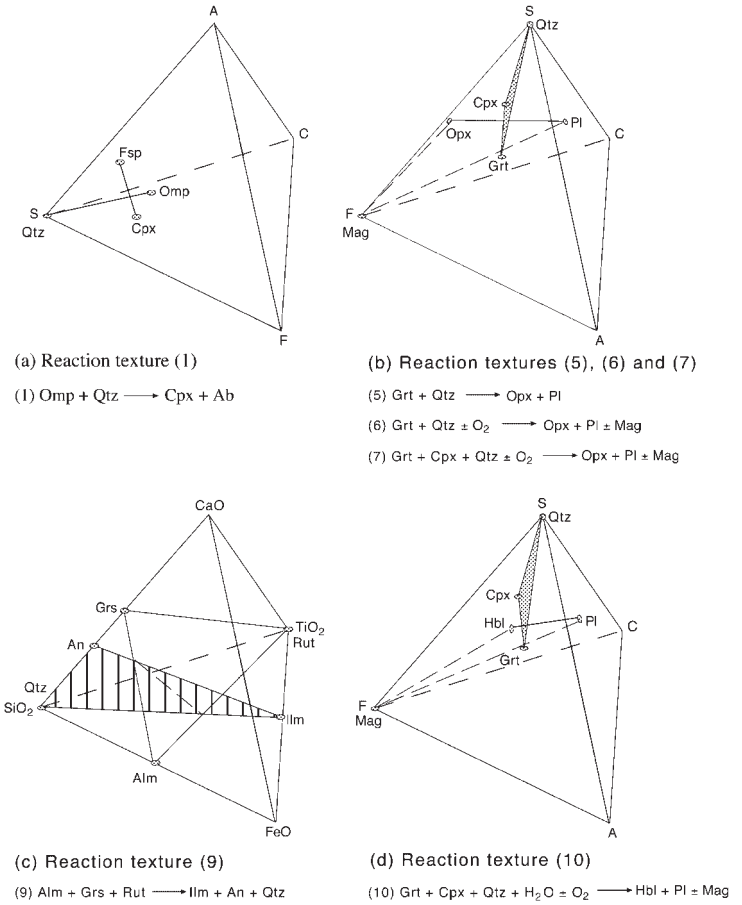

Fig. 9. Al_2O_3–SiO_2–(FeO + Mg)–(CaO + Na_2O) and CaO–SiO_2–FeO–TiO_2 diagrams showing possible metamorphic reactions occurring in the Hengshan high- and medium-pressure granulites. In (a), (b) and (d): A indicates Al_2O_3; S, SiO_2; F, FeO + Mg; C, CaO + Na_2O. Mineral symbols are after Kretz (1983).

analysis of *P–T* evolution constrained by reaction history and petrogenetic grids.

Two significant factors may hinder quantitative *P–T* determinations. They are: (1) different-scale chemical zoning, which may be the product of growth processes and/or diffusion that make it impossible to infer with certainty the compositions that were, at any time, in mutual equilibrium; (2) lack of general agreement about the calibration of individual conventional geothermobarometers, which are often not internally consistent with respect to thermodynamic properties. To reduce the influence of the first factor, we estimate the *P–T* conditions of the M_3 and M_4 assemblages based on chemically unzoned symplectic or coronitic minerals and the compositions of garnet just inwards of the outermost diffusional rims, assuming that these compositions have been in equilibrium. The *P–T* conditions of the peak assemblages (M_2) were estimated using the core compositions of garnet porphyroblasts and matrix-type plagioclase, clinopyroxene, orthopyroxene and hornblende.

To avoid the influence of the second factor, we calculate pressures and temperatures using *P–T* programs based on internally consistent thermodynamic databases, rather than traditional geothermobarometers. Of several *P–T* programs available, THERMOCALC (Powell & Holland, 1994; Holland & Powell, 1998) and TWQ (Berman, 1991) have been most widely used. Both programs calculate pressures and temperatures from the intersections of two or more end-member reactions in *P–T* space using one set of internally consistent thermodynamic data. A major difference between THERMOCALC and TWQ is that the former calculates average pressures and temperatures based on an independent set of equilibria, whereas the latter uses all possible equilibria to compute pressures and temperatures (Berman, 1991). In this study, the THERMOCALC program was used because it allows the likely uncertainties in the results of *P–T* calculations to be estimated, whereas the TWQ program does not allow the reliable calculation of uncertainties to be performed.

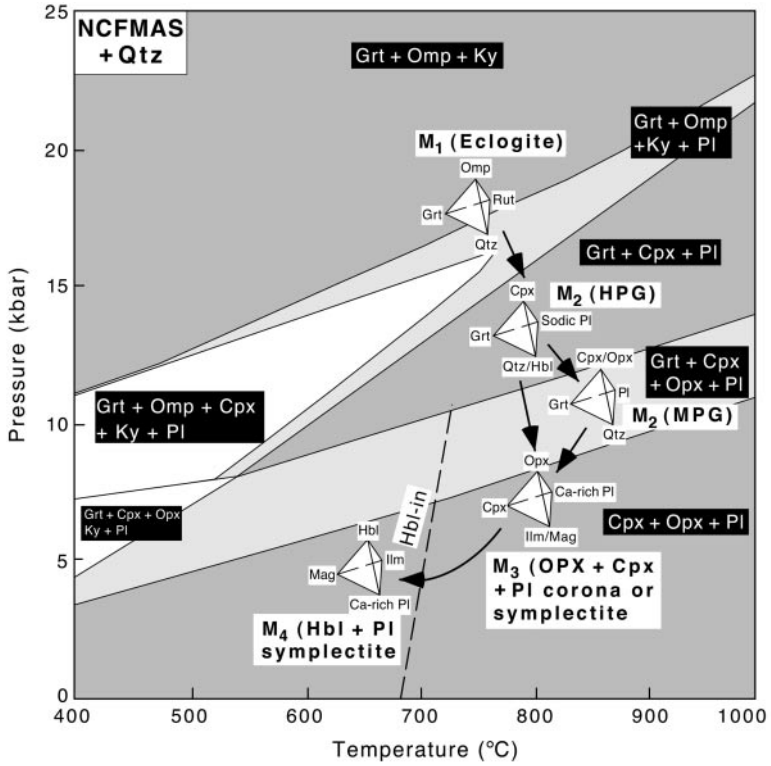

Fig. 10. *P–T* pseudosection for a portion of the NCFMAS system [after Holland & Powell (1998)] showing the qualitative *P–T* path of the high- and medium-pressure granulites constrained by the sequence of mineral assemblages. Divariant fields are in white, trivariant fields in light grey, quadrivariant fields in dark grey. Mineral symbols are after Kretz (1983).

Average *P–T* calculations followed the method of Powell & Holland (1994), using an updated and expanded version of the internally consistent Holland & Powell (1998) thermodynamic dataset and the computer program THERMOCALC version 2.75. Mineral activities were calculated for pyroxenes following Holland & Powell (1990), using an ideal two-site mixing model; for garnet following Berman (1990), using the ternary mixing model; for plagioclase activities using Darken's quadratic formulism (Holland & Powell, 1992); and for hornblende following Holland & Blundy (1994), using a non-ideal mixing model. Quartz was assumed to be pure.

To examine and reduce the effect of resetting of post-peak thermal events (M_3 and M_4), the *P–T* conditions of the peak assemblage (M_2) are estimated for both the core and rim compositions of garnet porphyroblast and matrix-type clinopyroxene, orthopyroxene, hornblende and plagioclase from those samples that are devoid of symplectites and coronas around embayed garnet grains. The complete end-member phases used in the calculations for the high-pressure granulites include anorthite, albite, pyrope, almandine, grossular, quartz, diopside, hedenbergite, Ca-Tschermak's pyroxene, tremolite, tschermakite, Fe-actinolite, pargasite, glaucophane and H_2O, which constitute eight independent equilibria (Table 6a). Samples A60 and A03 are devoid of hornblende, and thus only three independent equilibria [reactions (1)–(3) in Table 6a] are used in the calculations. These independent reactions from eight samples gave average *P–T* estimates of 13·4–15·5 kbar and 770–840°C and 8·2–10·7 kbar and 638–835°C for the core and rim compositions, respectively, of the peak minerals of the high-pressure granulites (Table 7). The results overlap at relatively large uncertainty, and most of their σ_{fit} values are over statistical limits (Powell & Holland, 1994). These may have resulted from resetting by post-peak thermal events (M_3 and M_4). Despite high uncertainties and large σ_{fit} values, eight samples from the high-pressure granulites yielded similar results and recorded a nearly isothermal decompression from core to rim compositions, except for sample B61, which gave a lower temperature estimate (638°C), probably reflecting resetting during the M_4 event.

The end-member phases of the peak assemblage (M_2) in the medium-pressure granulites are anorthite, pyrope, almandine, grossular, quartz, diopside, hedenbergite, Ca-Tschermak's pyroxene, ferrosilite, enstatite and Mg-Tschermak's pyroxene, which make up six independent equilibria (Table 6b). The *P–T* conditions estimated

Table 6: Independent equilibria used in THERMOCALC calculations

(a) Independent equilibria used for P–T *estimates of the peak assemblage (M_2) of the high-pressure granulite*

(1) q + cats = an
(2) 3an + 3di = py + 2gr + 3q
(3) 3an + 3hed = 2gr + alm + 3q
(4) 21an + 6tr = 10py + 11gr + 27q + $6H_2O$
(5) 2py + 4gr + 12q + 3ts = 12an + 3tr
(6) 21an + 6fact = 11gr + 10alm + 27q + $6H_2O$
(7) 9an + 9q + 6parg = 8py + 7gr + 6ab + $6H_2O$
(8) 2py + 4gr + 12q + 3gl = 6an + 6ab + 3tr

(b) Independent equilibria used for P–T *estimates of the peak assemblage (M_2) of the medium-pressure granulite and pyroxene + plagioclase symplectite and corona assemblage (M_3)*

(1) q + cats = an
(2) 3an + 3en = 3q + 2py + gr
(3) 3q + gr + 3mgts = 3an + py
(4) 3an + 3di = 3q + py + 2gr
(5) 3an + 3fs = 3q + gr + 2alm
(6) 3an + 3hed = 3q + 2gr + alm

(c) Independent equilibria used for P– T *estimates of hornblende + plagioclase symplectite*

(1) 5ts + 11q + 3gr = 3tr + 13an + $2H_2O$
(2) 3ts + 12q + 2py + 4gr = 3tr + 12an
(3) 6fact + 21an = $6H_2O$ + 27q + 11gr + 10alm
(4) 40ts + 11gl + 24gr = 13tr + 22parg + 82an + $16H_2O$
(5) 2parg + 8q = tr + ts + 2ab

Abbreviations: ab, albite; alm, almandine; an, anorthite; cats, Ca-Tschermak's pyroxene; di, diopside; en, enstatite; fact, Fe-actinolite; fs, ferrosilite; gr, grossular; gl, glaucophane; hed, hedenbergite; mgts, Mg-Tschermak's pyroxene; py, pyrope; para, pargasite; q, quartz; tr, tremolite; ts, tschermakite.

with these independent equilibria from seven medium-pressure granulites samples are 9–11 kbar and 820–870°C for the core compositions, and 7·0–8·0 kbar and 730–850°C for the rim compositions (Table 7). Compared with those of the high-pressure granulites, these results have relatively smaller uncertainties and σ_{fit} values, most of which are within statistical limits (Powell & Holland, 1994). As in the high-pressure granulites, the core-to-rim compositions of the peak minerals of medium-pressure granulites also recorded a near-isothermal decompression process.

To calculate the pressure and temperature of the orthopyroxene + plagioclase symplectites and clinopyroxene + orthopyroxene + plagioclase coronas (M_3), mineral analyses were taken from the rims of garnet porphyroblasts and associated symplectic or coronitic plagioclase, orthopyroxene and clinopyroxene grains that were devoid of chemical zoning. The end-member phases and independent equilibria are the same as those used for the *P–T* estimates of the M_2 assemblage in the medium-pressure granulites (Table 6b). For the orthopyroxene + plagioclase symplectite, only three independent equilibria [reactions (1)–(3) in Table 6b] could be used for their *P–T* estimates. The results of the average *P–T* calculations for 10 samples or microdomains are summarized in Table 8. These samples yielded *P–T* conditions of 6·5–7·5 kbar and 740–840°C (Table 9), with relatively large uncertainties and small σ_{fit} values.

Mineral analyses for the *P–T* estimates of the hornblende + plagioclase symplectite (M_4) were also taken from the rims of garnet porphyroblasts and associated chemically unzoned hornblende and plagioclase symplectites. The end-member phases are anorthite, albite, pyrope, almandine, grossular, quartz, tremolite, tschermakite, Fe-actinolite, pargasite, glaucophane and H_2O, and independent equilibria built up from these end-phases are listed in Table 6c. Nine samples or microdomains yielded similar results that fall in the range 4·0–6·0 kbar and 680–790°C (Table 9). These results overlap at smaller uncertainties and σ_{fit} values are within statistical limits (Powell & Holland, 1994).

P–T PATH

The combination of petrographic textures, mineral compositions, metamorphic reaction history, petrogenetic grids and thermobarometric data of the Hengshan granulites defines a near-isothermal decompressional clockwise *P–T* path as summarized in Fig. 11. Although the *P–T* conditions of the early prograde eclogite facies (M_1) cannot be quantitatively determined because of the absence of the major minerals, the remaining key part of the *P–T* path is well constrained by quantitative THERMOCALC estimates for the M_2, M_3 and M_4 assemblages. The establishment of this *P–T* path is based on the assumption that the reaction textures and mineral compositions used to determine the *P–T* path are related to a single metamorphic cycle rather than to two or more unrelated metamorphic events. A single-cycle granulite-facies model for the Hengshan granulites is favoured because there is no petrographic and chronological evidence suggesting the existence of a second regional metamorphic event. Furthermore, Kumar & Chacko (1994) suggested that even the minimum calculated dimensions of grain growth under regional metamorphic events of an ~10–50 Ma time scale are larger than the observed dimensions of most orthopyroxene, clinopyroxene and plagioclase symplectite grains (<0·2 mm in their longest dimension). Therefore, it seems unlikely that the relatively slow prograde heating path of a second regional metamorphic event would be conducive to the formation

Table 7: THERMOCALC results for the peak assemblage of the high- and medium-pressure granulites

Sample:	Core								Rim							
	T (°C)	*P* (kbar)	aH_2O	SD(*T*)	SD(*P*)	Correl.	Fit	NR	*T* (°C)	*P* (kbar)	aH_2O	SD(*T*)	SD(*P*)	Correl.	Fit	NR
	High-pressure granulites															
A12	810	14·1	1·0	93	2·2	0·545	1·62	8	808	8·5	1·0	96	1·9	0·324	1·66	8
B12	772	13·4	0·8	94	2·1	0·581	1·57	8	816	8·2	0·9	102	2·3	0·320	1·96	8
A60	811	14·7	—	119	2·3	0·831	0·27	3	803	10·7	—	116	1·7	0·674	0·43	3
A61	817	13·7	0·6	119	2·8	0·467	2·01	8	794	10·1	0·2	95	2·2	0·220	1·87	8
B61	811	14·6	0·5	88	2·2	0·465	1·58	8	638	8·8	1·0	113	2·4	0·338	2·29	8
A03	821	15·5	—	155	3·3	0·784	1·55	3	809	10·2	—	143	2·0	0·616	1·40	3
A40	841	13·6	1·0	127	2·7	0·437	2·22	8	832	9·0	1·0	126	2·1	0·329	1·95	8
B60	837	13·6	1·0	97	2·1	0·553	1·53	8	834	9·4	1·0	109	1·9	0·356	1·69	8
	Medium-pressure granulites															
C12	869	11·3	—	200	3·0	0·828	1·80	5	804	8·3	—	107	1·4	0·798	0·45	6
A75	845	10·3	—	146	2·3	0·714	1·57	5	820	8·5	—	96	1·4	0·635	1·07	6
B75	854	10·1	—	96	1·4	0·712	0·71	5	851	8·5	—	95	1·2	0·724	0·86	6
A13	818	9·3	—	106	1·5	0·787	0·89	6	773	7·6	—	83	1·2	0·654	0·83	6
B13	839	9·4	—	120	1·8	0·715	1·30	6	756	7·2	—	238	2·9	0·953	0·64	4
C75	843	10·3	—	100	1·4	0·775	0·96	6	727	7·3	—	84	1·1	0·741	0·56	5
C13	841	9·5	—	162	2·2	0·786	1·52	5	832	8·6	—	95	1·4	0·671	1·01	5

aH_2O gives the fluid composition used; —, reactions without H_2O; SD(*T*), standard deviations on temperature; SD(*P*), standard deviations on pressure; Correl., correlation between the uncertainties on *P* and *T*; Fit, a goodness-of-fit parameter describing the averaging of *n* equilibria (Powell & Holland, 1988); NR, the number of independent equilibria calculated by THERMOCALC.

Table 8: THERMOCALC results for pyroxene + plagioclase symplectite and corona

Sample	*T* (°C)	*P* (kbar)	SD(*T*)	SD(*P*)	Correl.	Fit	NR
13310	796	6·9	99	1·1	0·654	0·98	5
13301	762	7·2	126	1·6	0·839	0·86	4
7501	782	6·8	242	2·6	0·937	0·38	3
7508	758	6·8	296	3·2	0·965	0·31	3
7510	740	6·5	167	1·9	0·855	0·80	3
7517	827	7·5	191	2·2	0·897	0·59	3
7518	786	7·4	223	2·6	0·849	1·33	3
7523	801	7·3	207	2·4	0·847	1·27	3
7511	749	6·5	105	1·2	0·464	0·37	3
7531	836	6·8	123	1·3	0·403	0·65	3

Abbreviations as in Table 7.

Table 9: THERMOCALC results for hornblende + plagioclase symplectite

Sample	*T* (°C)	*P* (kbar)	aH_2O	SD(*T*)	SD(*P*)	Correl.	Fit	NR
6014	776	5·8	0·9	89	1·5	0·502	1·19	5
6101	685	4·3	0·1	88	1·0	0·418	1·13	5
6121	774	5·8	0·5	91	1·1	0·521	0·60	5
7504	765	4·6	0·4	85	1·3	0·386	0·69	5
7527	745	4·8	0·8	83	1·4	0·474	1·16	5
7528	767	4·6	0·6	88	1·4	0·427	1·10	5
1218	789	4·9	0·8	117	1·7	0·461	1·37	5
1331	746	4·1	0·4	88	1·3	0·409	1·30	5
1220	705	4·9	0·5	90	1·2	0·434	0·54	5

Abbreviations as in Table 7.

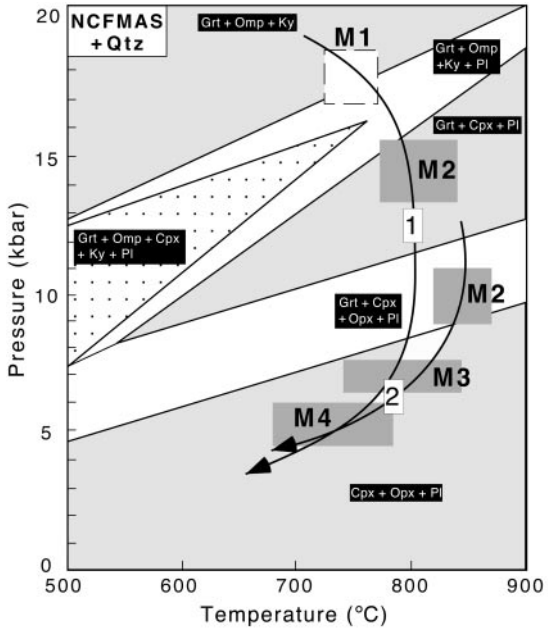

Fig. 11. *P–T* pseudosection of a portion of the NCFMAS system [(after Holland & Powell (1998)] illustrating the estimated *P–T* path of the high- and medium-pressure granulites from the Hengshan Complex. The dashed box shows the early prograde eclogite-facies metamorphism whose *P–T* conditions cannot be quantitatively estimated because of the absence of main minerals in this stage. 1, high-pressure granulites; 2, medium-pressure granulites. Mineral symbols are after Kretz (1983).

of the fine-grained symplectite minerals found in the Hengshan granulites.

Despite effects from resetting of Fe–Mg exchange equilibria during post-peak processes, the core compositions of the peak assemblage garnet + clinopyroxene + sodic plagioclase + quartz ± hornblende in the Hengshan high-pressure granulites preserve high-pressure granulite-facies conditions of 13·4–15·5 kbar and 770–840°C, and likewise, the core compositions of the peak assemblage of orthopyroxene + clinopyroxene + garnet + plagioclase + quartz in the medium-pressure granulites preserve medium-pressure granulite-facies conditions of 9–11 kbar and 820–870°C. The obtained high-pressure conditions are supported by the presence of grossular-rich cores in garnet porphyroblasts and albite-rich cores in matrix plagioclases in high-pressure granulites. The THERMOCALC results also reveal that core-to-rim compositional variations of the peak minerals in high- and medium-pressure granulites reflect a nearly isothermal decompression process. Also, the rim compositions of the peak assemblage in the high-pressure granulites yielded *P–T* conditions similar to those estimated for the core compositions of the peak assemblage in the medium-pressure granulites. This suggests that the high-pressure granulites may have undergone medium-pressure granulite-facies metamorphism following the high-pressure event, and that the medium-pressure granulites in the Hengshan Complex may have resulted from retrograded high-pressure granulites.

Medium- to low-pressure granulite-facies conditions of 6·5–8·0 kbar and 750–830°C estimated for the pyroxene + plagioclase corona or symplectite assemblage (M_3) suggest nearly isothermal decompression from the peak

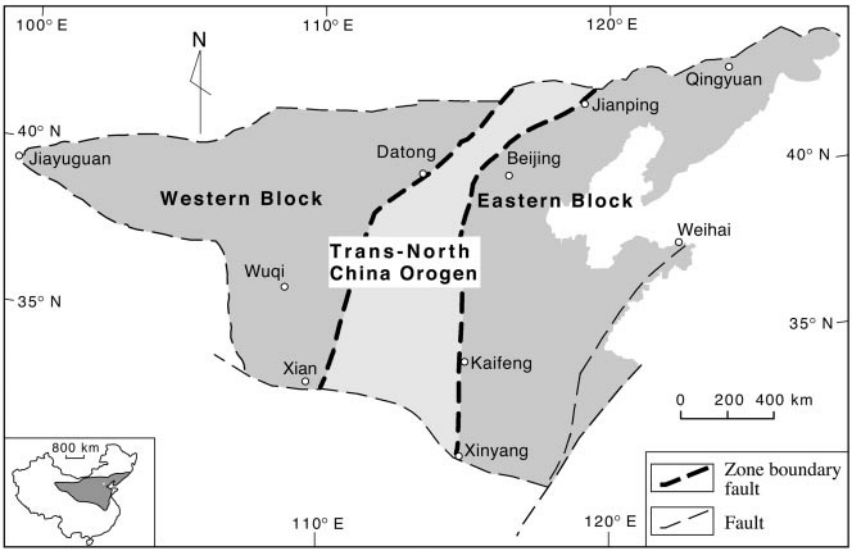

Fig. 12. Sketch map showing locations of the Archaean eastern and western blocks, which are separated by the early Proterozoic Trans-North China Craton.

M_2 assemblage (Fig. 11). Harley (1989) displayed various mineral reaction textures that could be expected in rocks that have experienced nearly isothermal decompression. He noted that orthopyroxene + plagioclase symplectites around embayed garnet grains are characteristic of mafic granulites that have undergone near-isothermal decompression. Near-isothermal decompression paths require that unroofing of deep-seated metamorphic rocks is rapid relative to the rate of thermal relaxation and cooling. This can typically be accomplished by rapid erosional exhumation or extensional faulting (England & Richardson, 1977; England & Thompson, 1984; Thompson & England, 1984; Oxburgh, 1989; Brown, 1993).

The *P–T* conditions of 4·5–6·0 kbar and 680–790°C estimated for hornblende + plagioclase symplectite (M_4) indicate further decompression accompanied by cooling and retrogression that is represented by the presence of hydrous phase minerals in this assemblage. The M_4 assemblage probably formed when the metamorphic terrane was being exhumed to a shallower level, and hence, the pressure and temperature were simultaneously decreasing.

GEOTECTONIC IMPLICATIONS

The North China Craton is not well constrained in terms of its tectonic evolution. Traditionally, it has been considered to be composed of a uniform Archaean to Early Proterozoic basement, overlain by younger cover, and its tectonic history was explained using a pre-plate tectonic model (Huang, 1977). Terrane accretion and collision models have only recently been applied, including recognition of a Palaeoproterozoic orogen—the Trans-North China Orogen, which separates the craton into eastern and western blocks (Fig. 12; Zhao *et al.*, 1999*b*, 1999*c*). The western block has a double-layered basement, with the late Archaean TTG gneisses and supracrustal rocks overlain by Early Proterozoic khondalites, which mainly crop out along the boundary with the Trans-North China Orogen. The Archaean TTG gneisses and supracrustal rocks experienced metamorphism at ~2·5 Ga, with isobaric cooling (IBC) anticlockwise *P–T–t* paths, suggesting an origin related to the intrusion and underplating of mantle-derived magmas, whereas the Early Proterozoic khondalites underwent metamorphism at ~1·8 Ga, with near-isothermal decompressional clockwise *P–T–t* paths, suggesting an origin related to continental collision (Zhao *et al.*, 1999*c*). The eastern block is composed predominantly of Middle to Late Archaean TTG gneisses and syn-tectonic granitoids, with minor rafts or sheets of Early to Middle Archaean supracrustal rocks including ultramafic to felsic volcanic rocks and metasediments. The TTG gneisses make up >80% of the basement and the structural style is dominated by ovoid domes, separated by linear belts. All these rocks underwent regional metamorphism at ~2·5 Ga, with anticlockwise *P–T–t* paths (Zhao *et al.*, 1998). Intervening between the western and eastern blocks is the Trans-North China Orogen. The orogen consists of a series of low-grade and high-grade belts containing reworked Archaean components and juvenile Early Proterozoic igneous and sedimentary rocks. Geochemical and geochronological studies show that these rocks developed in magmatic arc and intra-arc basin environments (Bai *et al.*, 1992; Wang *et al.*, 1996), and experienced regional metamorphism at ~1·9–1·8 Ga (Wilde *et al.*, 1997, 1998; Zhao *et al.*, 2000; A. Kröner, personal communication, 1999).

This study reports the presence of 1·9–1·8 Ga high-pressure granulites from the Hengshan Complex in the Trans-North China Orogen. The high-pressure granulites (or retrograded eclogites) from the Hengshan Complex are petrologically and geochronologically similar to those found in the Huaian (Zhai *et al.*, 1992, 1995; Guo *et al.*, 1993), Xuanhua (Wang *et al.*, 1994) and Northern Hebei (Li *et al.*, 1998) Complexes elsewhere in the orogen. They constitute a NE–SW-trending high-pressure granulite belt, tens of kilometres wide and up to 500 km long, in the northern part of the Trans-North China Orogen. The southern part of the orogen is occupied by a high-pressure amphibolite belt along which 10–14 kbar garnet amphibolites and kyanite–staurolite–anthophyllite mafic schist occur (Wang *et al.*, 1997; Zhao, 2001). This high-pressure amphibolite belt seems to be the tectonic counterpart of the high-pressure granulite belt discussed in this paper, and they together constitute a large-scale Early Proterozoic high-pressure belt that traverses the orogen and represents an important terrane boundary. The existence of this high-pressure belt is important because it suggests that Phanerozoic-style geodynamic processes operated far back in Early Proterozoic time in the North China Craton.

The *P–T* path established for the high-pressure granulites in the Hengshan Complex, along with data on the tectonothermal evolution of the other complexes in the Trans-North China Orogen, places important constraints on the tectonic setting of the orogen and in evaluating tectonic models for the evolution of the North China Craton. The estimated *P–T* path for the high- and medium-pressure granulites from the Hengshan Complex suggests a tectonothermal event that involved an initial phase of crustal thickening in M_1, followed by nearly isothermal exhumation in M_2 and M_3, and cooling and retrogression during M_4. This tectonothermal history was likewise shared by the Wutai and Fuping Complexes and other tectonic complexes in the Trans-North China Orogen (Zhai *et al.*, 1992, 1995; Guo *et al.*, 1993; Wang *et al.*, 1994; Li *et al.*, 1998; Zhao *et al.*, 1999*a*, 2001).

Thus, rather than metamorphism and deformation of the Hengshan Complex being related to localized interaction with the Fuping and Wutai Complexes, through closure of either an intracratonic rift (Tian, 1991; Yuan & Zhang, 1993) or a large ocean (Li *et al.*, 1990; Bai *et al.*, 1992; Wang *et al.*, 1996), we consider the Hengshan Complex, along with the Fuping, Wutai and other complexes in the Trans-North China Orogen, to be part of a single system that was accreted to the North China Craton during the collision between the eastern and western blocks, resulting in the final assembly of the North China Craton at $\sim$1·8 Ga.

ACKNOWLEDGEMENTS

We thank E. Essene and R. Powell for their helpful and critical comments on an earlier version of this paper, as well as A. Kröner, K. Y. Wang, M. G. Zhai and S. W. Liu for numerous discussions. The work was financially supported by an NSFC Grant to L.Z.L. (No. 49772144), an ARC Large Grant to S.A.W. and P.A.C. (No. A39532446), and Tectonics Special Research Centre Funds to P.A.C. This is Tectonics Special Research Centre Publication No. 74.

REFERENCES

Bai, J., Wang, R. Z. & Guo, J. J. (1992). *The Major Geologic Events of Early Precambrian and their Dating in Wutaishan Region*. Beijing: Geological Publishing House (in Chinese with English abstract).

Baker, A. J. (1990). *Introduction to Metamorphic Textures and Microstructures*. Glasgow: Blackie.

Berman, R. G. (1990). Mixing properties of Ca–Mg–Fe–Mn garnets. *American Mineralogist* **75**, 328–344.

Berman, R. G. (1991). Thermobarometry using multi-equilibrium calculations: a new technique, with petrological applications. *Canadian Mineralogist* **29**, 833–855.

Bohlen, S. R. (1991). On the formation of granulites. *Journal of Metamorphic Geology* **9**, 223–229.

Bohlen, S. R. & Liotta, J. (1986). A barometer for garnet amphibolites and garnet granulites. *Journal of Petrology* **27**, 1025–1034.

Brown, M. (1993). *P–T–t* evolution of mountain belts and the causes of regional metamorphism. *Journal of the Geological Society, London* **150**, 227–241.

Droop, G. T. R. (1987). A general equation for estimating Fe^{3+} concentrations in ferromagnesian silicates and oxides from microprobe analyses, using stoichiometric criteria. *Mineralogical Magazine* **51**, 431–435.

England, P. C. & Richardson, S. W. (1977). The influence of erosion upon the mineral facies of rocks from different metamorphic environments. *Journal of the Geological Society, London* **134**, 3201–3213.

England, P. C. & Thompson, A. B. (1984). Pressure–temperature–time paths of regional metamorphism, I. Heat transfer during the evolution of regions of thickened continental crust. *Journal of Petrology* **25**, 894–928.

Essene, E. J. (1989). The current status of thermobarometry in metamorphic rocks. In: Daly, J. S., Cliff, R. A. & Yardley, B. W. D. (eds) *Evolution of Metamorphic Belts*. *Geological Society, London, Special Publication* **43**, 1–44.

Guo, J. H., Zhai, M. G. & Zhang, Y. G. (1993). Early Precambrian Manjinggou high-pressure granulites melange belt on the southern edge of the Huaian Complex, North China Craton: geological features, petrology and isotopic geochronology. *Acta Petrologica Sinica* **9**, 329–341 (in Chinese with English abstract).

Hansen, B. (1981). The transition from pyroxene granulite facies to garnet clinopyroxene granulite facies: experiments in the system $CaO–MgO–Al_2O_3–SiO_2$. *Contributions to Mineralogy and Petrology* **76**, 234–242.

Harley, S. L. (1989). The origins of granulites: a metamorphic perspective. *Geological Magazine* **126**, 215–247.

Harley, S. L. (1992). Proterozoic granulite terranes. In: Condie, K. C. (ed.) *Proterozoic Crustal Evolution*. Amsterdam: Elsevier, pp. 301–360.

Heinrich, C. A. (1982). Kyanite-eclogite to amphibolite facies evolution of hydrous mafic and pelitic rocks, Adula Nappe, central Alps. *Contributions to Mineralogy and Petrology* **81**, 30–38.

Hill, R. I., Campbell, I. R., Davis, G. F. & Griffiths, R. W. (1992). Mantle plumes and continental tectonics. *Science* **256**, 186–193.

Holland, T. J. B. & Blundy, J. (1994). Non-ideal interactions in calcic amphiboles and their bearing on amphibole–plagioclase thermometry. *Contributions to Mineralogy and Petrology* **116**, 433–447.

Holland, T. J. B. & Powell, R. (1990). An internally consistent thermodynamic dataset with uncertainties and correlations: the system $Na_2O–K_2O–CaO–MgO–MnO–FeO–Fe_2O_3–Al_2O_3–SiO_2–TiO_2–C–H_2–O_2$. *Journal of Metamorphic Geology* **8**, 89–124.

Holland, T. J. B. & Powell, R. (1992). Plagioclase feldspar activity–composition relations based on Darken's Quadratic Formalism and Landau theory. *American Mineralogist* **77**, 53–61.

Holland, T. J. B. & Powell, R. (1998). An internally consistent thermodynamic data set for phases of petrological interest. *Journal of Metamorphic Geology* **16**, 309–343.

Huang, J. Q. (1977). The basic outline of China tectonics. *Acta Geologica Sinica* **52**, 117–135 (in Chinese).

Kretz, R. (1983). Symbols for rock-forming minerals. *American Mineralogist* **68**, 277–279.

Kumar, G. R. R. & Chacko, T. (1991). Geothermobarometry of mafic granulites and metapelite from the Palghat Gap, South India: petrological evidence for isothermal uplift and rapid cooling. *Journal of Metamorphic Geology* **12**, 479–492.

Leake, B. E. (1997). Nomenclature of amphiboles: report of the Subcommittee on Amphiboles of the International Mineralogical Association, Commission on New Minerals and Mineral Names. *American Mineralogist* **82**, 1019–1037.

Li, J. H., Zhai, M. G., Li, Y. G. & Zhan, Y. G. (1998). Discovery of Late Archean high-pressure granulites in Luanping–Chengde area, Northern Hebei Province: tectonic implications. *Acta Petrologica Sinica* **14**, 34–41 (in Chinese with English abstract).

Li, J. L., Wang, K. Y., Wang, Q. C., Liu, X. H. & Zhao, Z. Y. (1990). Early Proterozoic collision mountain belt in Wutaishan area, China. *Scientia Geologica Sinica* **25**, 1–11 (in Chinese with English abstract).

Ma, X. Y., Bai, J., Shuo, S. T., Lao, Q. Y. & Zhang, J. S. (1987). *The Early Precambrian Tectonic Framework of China and Research Methods*. Beijing: Geological Publishing House (in Chinese).

Mengel, F. & Rivers, T. (1991). Decompression reactions and *P–T* conditions in high-grade rocks, Northern Labrador: *P–T–t* paths from individual samples and implications for Early Proterozoic tectonic evolution. *Journal of Petrology* **32**, 139–167.

Moecher, D. P., Anovitz, L. M. & Essene, E. J. (1988). Calculation of clinopyroxene–garnet–plagioclase–quartz geobarometers and application to high grade metamorphic rocks. *Contributions to Mineralogy and Petrology* **100**, 92–106.

Möller, C. (1998). Decompressed eclogites in the Sveconorwegian (-Grenvillian) orogen of SW Sweden: petrology and tectonic implications. *Journal of Metamorphic Geology* **16**, 641–656.

Mueller, R. F. & Saxena, S. K. (1977). *Chemical Petrology with Applications to the Terrestrial Planets and Meteorites*. New York: Springer.

Newton, R. C. & Perkins, D. (1982). Thermodynamic calibration of geobarometer. In: Newton, R. C., Navrotsky, A. & Wood, B. J. (eds) *Thermodynamics of Minerals and Melts*. New York: Springer, pp. 129–145.

O'Brien, P. J. (1989). The petrology of retrograded eclogites of the Oberpfalz Forest, northeastern Bavaria, West Germany. *Tectonophysics* **157**, 195–213.

Oxburgh, E. R. (1989). Some thermal aspects of granulite history. In: Vielzeuf, D. & Vidal, P. H. (eds) *Granulites and Crustal Evolution*. Dordrecht: Kluwer Academic, pp. 569–580.

Perkins, D. & Chipera, S. J. (1985). Garnet–orthopyroxene–plagioclase–quartz barometry: refinement and application to the English River subprovince and the Minnesota River Valley. *Contributions to Mineralogy and Petrology* **89**, 69–80.

Powell, R. & Holland, T. J. B. (1994). Optimal geothermometry and geobaromemetry. *American Mineralogist* **79**, 120–133.

Rubie, D. C. (1990). Role of kinetics in the formation and preservation of eclogites. In: Carswell, D. A. (ed.) *Eclogite Facies Rocks*. Glasgow: Blackie, pp. 111–140.

Sandiford, M. & Powell, R. (1986). Deep crustal metamorphism during continental extension: ancient and modern examples. *Earth and Planetary Science Letters* **79**, 151–158.

Smelov, A. P. & Beryozkin, V. I. (1993). Retrograded eclogites in the Olekma granite–greenstone region, Aldan Shield, Siberia. *Precambrian Research* **62**, 419–430.

Thompson, A. B. & England, P. C. (1984). Pressure–temperature–time paths of regional metamorphism, II. Their influences and interpretation using mineral assemblages in metamorphic rocks. *Journal of Petrology* **25**, 929–955.

Thost, D. E., Hensen, B. J. & Motoyoshi, Y. (1991). Two-stage decompression in garnet-bearing mafic granulites from Sostrene Island, Prydz Bay, East Antarctica. *Journal of Metamorphic Geology* **9**, 245–256.

Tian, Y. Q. (1986). A preliminary study on the petrogenesis of the Hengshan grey gneisses. *Shanxi Geology* **2**, 95–113 (in Chinese with English abstract).

Tian, Y. Q. (1991). *Geology and Mineralzation of Wutai–Hengshan Greenstone Belt*. Taiyuan: Shanxi Science and Technology Press (in Chinese).

Tian, Y. Q. (1992). Geochronology and Nd isotopic evolution of the Hengshan Complex. *Geochimica* **3**, 255–263 (in Chinese with English abstract).

Vernon, R. H. (1996). Problems with inferring *P–T–t* paths in low-*P* granulites facies rocks. *Journal of Metamorphic Geology* **14**, 143–154.

Wang, K. Y., Hao, J., Cawood, P. & Wilde, S. A. (1997). High-pressure metamorphism in kyanite-bearing schists from the original Jinganku Formation of the Wutaishan. *Proceedings of the 30th International Geological Conference: Precambrian Geology and Metamorphic Petrology* **17**, 213–220.

Wang, R. M., Lai, X. Y., Dong, W. D., Ma, J. & Tang, B. (1994). Some evidence for the late Archean collisional belt in the western Hebei Province. In: Qian, X. L. & Wang, R. (eds) *Geological Evolution of the Granulite Terrains in the Part of the North China Craton*. Beijing: Seismological Press, pp. 7–20.

Wang, K. Y., Li, J. L., Hao, J., Li, J. H. & Zhou, S. P. (1996). The Wutaishan mountain belt within the Shanxi Province, Northern China: a record of late Archaean collision tectonics. *Precambrian Research* **78**, 95–103.

Wells, P. R. A. (1980). Thermal models for magmatic accretion and subsequent metamorphism of continental crust. *Earth and Planetary Science Letters* **46**, 253–265.

Wilde, S. A., Cawood, P. & Wang, K. Y. (1997). The relationship and timing of granitoid evolution with respect to felsic volcanism in the Wutai Complex, North China Craton. *Proceedings of the 30th International Geological Conference: Precambrian Geology and Metamorphic Petrology* **17**, 75–88.

Wilde, S. A., Cawood, P., Wang, K. Y. & Nemchin, A., (1998). SHRIMP U–Pb zircon dating of granites and gneisses in the Taihangshan–Wutaishan area: implications for the timing of crustal growth in the North China craton. *Abstracts of the 9th International Conference on Geochronology, Cosmochronology and Isotope Geology, Beijing. Chinese Science Bulletin* **43**, 144.

Yardley, B. W. D. (1989). *An Introduction to Metamorphic Petrology*. Harlow, UK: Longman.

Yuan, G. P. & Zhang, R. Y. (1993). The structural environment of the Palaeorift in the Wutai greenstone belt. *Shanxi Geology* **8**, 21–28 (in Chinese with English abstract).

Zhai, M. G., Guo, J. H. & Yan, Y. H. (1992). Discovery and preliminary study of the Archean high-pressure granulites in the North China. *Science in China* **12**, 1325–1330.

Zhai, M. G., Guo, J. H., Li, Y. G. & Yan, Y. H. (1995). Discovery of Archean retrograded eclogites in the North China Craton and their tectonic implications. *Chinese Science Bulletin* **40**, 1590–1594.

Zhao, G. C. (2001). Palaeoproterozoic amalgamation of the North China Craton. *Geological Magazine* **138**, 87–91.

Zhao, G. C., Wilde, S. A., Cawood, P. A. & Lu, L. Z. (1998). Thermal evolution of Archean basement rocks from the eastern part of the North China craton and its bearing on tectonic setting. *International Geology Review* **40**, 706–721.

Zhao, G. C., Cawood, P. A. & Lu, L. Z. (1999*a*). Petrology and *P–T* history of the Wutai amphibolites: implications for tectonic evolution of the Wutai Complex, China. *Precambrian Research* **93**, 181–199.

Zhao, G. C., Wilde, S. A., Cawood, P. A. & Lu, L. Z. (1999*b*). Thermal evolution of two textural types of mafic granulites in the North China craton: evidence for both mantle plume and collisional tectonics. *Geological Magazine* **136**, 223–240.

Zhao, G. C., Wilde, S. A., Cawood, P. A. & Lu, L. Z. (1999*c*). Tectonothermal history of the basement rocks in the western zone of the North China Craton and its tectonic implications. *Tectonophysics* **310**, 223–240.

Zhao, G. C., Wilde, S. A., Cawood, P. A. & Lu, L. Z. (2000). Petrology and *P–T* path of the Fuping mafic granulites: implications for tectonic evolution of the central zone of the North China Craton. *Journal of Metamorphic Geology* **18**, 375–391.

Zhao, G. C., Wilde, S. A., Cawood, P. A., Sun, M. & Lu, L. Z. (2001). Archaean blocks and their boundaries in the North China Craton: lithological, geochemical, structural and *P–T* path constraints. *Precambrian Research* **107**, 45–73.